



## Nutrient-limited growth with non-linear cell diffusion as a mechanism for floral pattern formation in yeast biofilms

Alexander Tam <sup>a,\*</sup>, J. Edward F. Green <sup>a</sup>, Sanjeeva Balasuriya <sup>a</sup>, Ee Lin Tek <sup>b</sup>, Jennifer M. Gardner <sup>b</sup>, Joanna F. Sundstrom <sup>b</sup>, Vladimir Jiranek <sup>b</sup>, Benjamin J. Binder <sup>a</sup>

<sup>a</sup> School of Mathematical Sciences, University of Adelaide, Adelaide, SA 5005, Australia

<sup>b</sup> Department of Wine and Food Science, Waite Campus, University of Adelaide, Urrbrae, SA 5064, Australia

### ARTICLE INFO

#### Article history:

Received 4 September 2017

Revised 1 April 2018

Accepted 3 April 2018

Available online 7 April 2018

#### Keywords:

Saccharomyces cerevisiae  
Mat formation experiment  
Angular pair-correlation function  
Reaction-diffusion  
Travelling wave solution  
Geometric singular perturbation theory  
Linear stability analysis

### ABSTRACT

Previous experiments have shown that mature yeast mat biofilms develop a floral morphology, characterised by the formation of petal-like structures. In this work, we investigate the hypothesis that nutrient-limited growth is the mechanism by which these floral patterns form. To do this, we use a combination of experiments and mathematical analysis. In mat formation experiments of the yeast species *Saccharomyces cerevisiae*, we observe that mats expand radially at a roughly constant speed, and eventually undergo a transition from circular to floral morphology. To determine the extent to which nutrient-limited growth can explain these features, we adopt a previously proposed mathematical model for yeast growth. The model consists of a coupled system of reaction-diffusion equations for the yeast cell density and nutrient concentration, with a non-linear, degenerate diffusion term for cell spread. Using geometric singular perturbation theory and numerics, we show that the model admits travelling wave solutions in one dimension, which enables us to infer the diffusion ratio from experimental data. We then use a linear stability analysis to show that two-dimensional planar travelling wave solutions for feasible experimental parameters are linearly unstable to non-planar perturbations. This provides a potential mechanism by which petals can form, and allows us to predict the characteristic petal width. There is good agreement between these predictions, numerical solutions to the model, and experimental data. We therefore conclude that the non-linear cell diffusion mechanism provides a possible explanation for pattern formation in yeast mat biofilms, without the need to invoke other mechanisms such as flow of extracellular fluid, cell adhesion, or changes to cellular shape or behaviour.

© 2018 Elsevier Ltd. All rights reserved.

### 1. Introduction

In nature, micro-organisms such as bacteria and fungi often live in large, multi-cellular colonies. Within these, interactions between cells and their environment can give rise to complex spatio-temporal structures. In cell biology research, considerable work has focused on hypothesising mechanisms that could be responsible for this pattern formation (see for example Asally et al., 2012; Ben-Jacob et al., 2000; Chen et al., 2014; Giverso et al., 2015; Klapper and Dockery, 2010; Reynolds and Fink, 2001; Reynolds et al., 2008; Smith et al., 2016; Tronnolone et al., 2017; Váčová et al., 2011; Xue et al., 2011). Due to the complexity of the biological processes and interactions, elucidating the extent to which each proposed mechanism is responsible for the observed patterns can be chal-

lenging even for single-cell organisms such as yeast. Indeed, it is inconceivable that we can construct a complete description of the relevant biological processes that is mathematically tractable. However, we can use simple models that retain relatively few features to predict whether particular mechanisms can drive the observed behaviour. This ability of mathematical models to decouple complex processes provides insight and predictive power that is often not possible using experiments alone (Murray, 2002).

A biofilm is one of the most common structures formed by communities of micro-organisms. In a biofilm, microbes reside within a self-produced matrix of extracellular polymeric substances (EPS), and adhere to a substrate. Biofilms help microbes to survive in several ways. For example, they contain channels that assist the transportation of nutrients and water (Váčová et al., 2011). In addition, the extracellular matrix protects microbes by preventing penetration of harmful external substances (Beauvais et al., 2009). Indeed, biofilms are notoriously resistant to anti-microbial therapy (Ramage et al., 2010),

\* Corresponding author.

E-mail address: [alexander.tam@adelaide.edu.au](mailto:alexander.tam@adelaide.edu.au) (A. Tam).

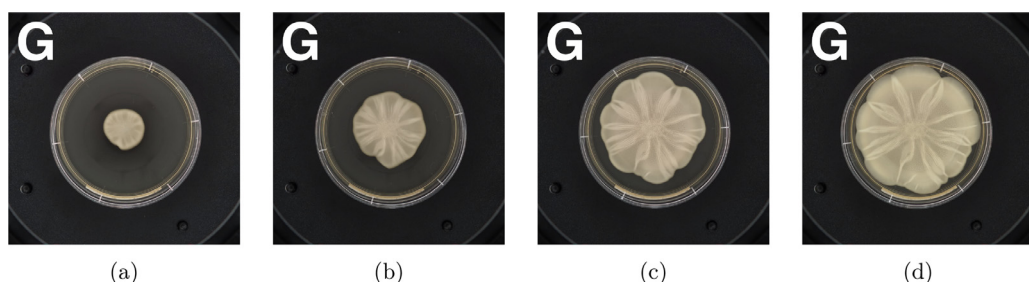


**Fig. 1.1.** A time series of images for a *S. cerevisiae* mat formation experiment. Photographs taken after approximately (a) 68 h, (b) 117 h, (c) 164 h, and (d) 237 h of incubation.

which contributes to the growing problem of anti-microbial resistance. Owing to their ubiquity and importance to many infections, biofilms have attracted much attention in cell biology research.

Although bacterial biofilms have been widely studied, less is known about pattern formation mechanisms during biofilm expansion of fungal organisms such as yeast (Chen et al., 2014). This is despite the fact that the bakers' yeast, *Saccharomyces cerevisiae*, is a common model organism in cell biology. As a eukaryotic organism, its cellular structure has similar features to more complex human and plant cells, such as a distinct nucleus and compartmentalised sub-cellular organelles, which is not the case for prokaryotic bacteria. Due to this, yeast is a useful model for investigating the mechanisms of morphogenesis, which is an important question in modern developmental biology (Murray, 2003). In addition, the *S. cerevisiae* genome has been sequenced (Goffeau et al., 1996), with many more strains being added, and a wide array of genetic tools such as mutant libraries are available. Uncovering the mechanisms of yeast growth is also of interest, for example, because yeasts contain cell division genes that are important in the development of cancer (Chen et al., 2014). In many situations, it would also be advantageous to develop methods to control yeast growth. For example, yeasts are used extensively in food and drink production, and in biotechnology. Furthermore, yeast biofilms commonly grow on indwelling medical devices such as catheters, stents, and prostheses. These biofilms are a leading cause of infections in clinical settings, and are particularly threatening to immunocompromised people (Martinez and Fries, 2010). In all of these cases, understanding of the underlying mechanisms is required to effectively control the growth.

In yeast biofilm formation experiments, *S. cerevisiae* cells are inoculated on a low density agar-filled Petri dish containing rich nutrients, including glucose and nitrogen. Initially, cells form a thin round biofilm, referred to as a mat (Fig. 1.1(a)). After growing for several days, mats can undergo a transition to a spatially non-uniform complex structure, characterised by the formation of petals (Reynolds and Fink, 2001), as shown in Fig. 1.1(b)–(d). We seek to understand the mechanisms governing the formation of this pattern, which we refer to as a floral morphology.

Mechanisms hypothesised to contribute to floral morphology fall into two categories (Chen et al., 2014). As yeast cells are non-motile, mats expand by the growth of new cells at their perimeter. Cellular growth requires access to nutrients, and therefore consumption and diffusion of nutrients may contribute to the pattern. In addition, mechanical interactions between cells and their environment are also thought to contribute to floral pattern formation. For example, fluid in the extracellular matrix is hypothesised to reduce friction between the cells and substrate, enabling mat biofilms to grow via a sliding motility (Reynolds and Fink, 2001). In other experiments, cells adhere strongly to the agar substrate, and mats demonstrate wrinkling that is aligned with the floral pattern (Chen et al., 2014). The complexity of these interacting mech-

anisms makes it difficult to derive a tractable mathematical model that includes all features simultaneously.

In this work, we neglect biofilm mechanics, and focus on the hypothesis that nutrient-limited growth is the mechanism by which petals form. To investigate this, we adopt a minimal mathematical model for mat growth. Our model takes the form of a coupled system of reaction–diffusion equations, with a non-linear, degenerate diffusion term for the spread of cells. The simplicity of the model ensures that we are able to estimate the relevant parameters from yeast mat formation experiments. This enables us to isolate the extent to which nutrient-limited growth alone contributes to the floral morphology.

The remainder of the article is structured as follows. In Section 2, we describe and quantify our mat formation experiments. Analysis of experimental images shows that the mat expands radially at a roughly constant speed, and that petals emerge following a period of near-uniform growth. In Section 3, we present the minimal reaction–diffusion model for nutrient-limited mat formation, and estimate all parameters except the diffusion ratio from experimental data. In Section 4, we exploit the fact that mats expand at a roughly constant speed to construct one-dimensional travelling wave solutions to the model. We use a combination of geometric singular perturbation theory and numerics to show that such solutions exist, and estimate the diffusion ratio using the speed of mat expansion. In Section 5, we apply the linear stability analysis of Müller and van Saarloos (2002), which shows that two-dimensional planar travelling waves are linearly unstable for the experimental range of parameters. We use this to predict the characteristic petal width, and verify the analysis by computing numerical solutions to the full model. We close the paper with a discussion in Section 6, and conclusion in Section 7.

## 2. Mat formation experiments

To generate and quantify the floral morphology, we produced two assays of the *S. cerevisiae* wine yeast strain L2056, yielding a total of thirteen mat biofilms. For each mat preparation, we inoculated 5000 cells on a 90 mm Petri dish filled with Yeast Peptone Dextrose (2% Bacto peptone, 1% yeast extract, 2% glucose) solidified with 0.3% agar. We then incubated each plate at 25°C. To capture the progress of mat formation, we took four images using the ProtoCOL 3 system (Synbiosis), after approximately 68, 117, 164, and 237 h of incubation. An example series of these images is shown in Fig. 1.1, and the remainder are presented in Appendix A. Fig. 1.1 illustrates the features of mat growth that we wish to understand. As shown, the mat initially expands in a near uniform circular manner. Eventually, the more complex floral morphology emerges, characterised by the formation of petals that become larger over time (Fig. 1.1(b)–(d)). Previous mat formation experiments with yeast, for example those of Reynolds and Fink (2001) and Chen et al. (2014), demonstrate similar behaviour. In this work, we investigate the extent to which a mathematical model that incorporates nutrient-limited growth alone can explain

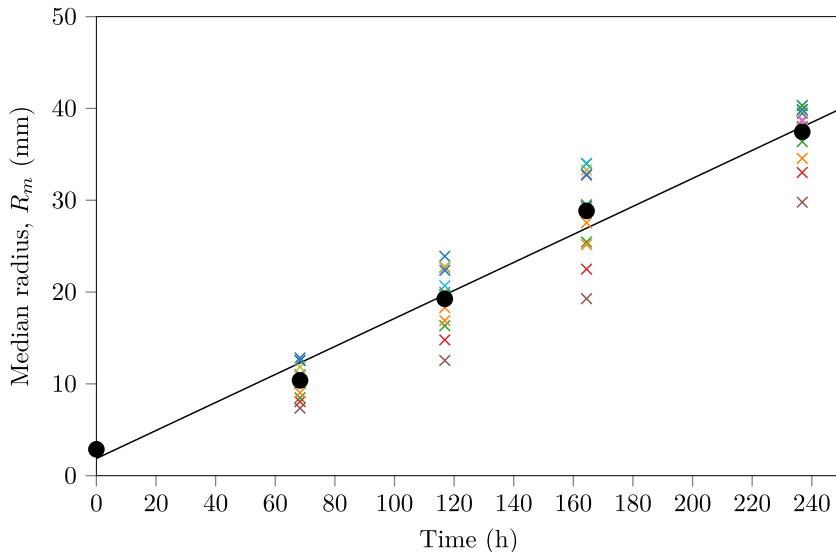


**Fig. 2.1.** The median radius,  $R_m$ , of mats computed from experimental images. The crosses indicate data points from individual experiments, and the dots indicate mean data for each time. The line is a linear least squares fit to the mean data. The coefficient of determination for the linear regression is  $r^2 = 0.9887$ .

the speed of mat expansion, and the transition to floral morphology.

### 2.1. Quantifying spatial patterns

Before formulating the model, we require a method of processing the images and quantifying the experimental patterns. First, we apply the `imbinarize` Matlab function to each photograph, which uses Otsu's method to convert them to binary images. Where necessary, we manually remove the border of the Petri dish from the image, so that only the mat remains. The binary image pixels define a two-dimensional square domain  $\mathcal{D}$ , consisting of an integer lattice with unit spacing. At any time  $t$ , the lattice sites  $(x, y) \in \mathcal{D}$  are either occupied by yeast cells, or unoccupied. This definition enables us to compute the mat centroid  $(\bar{x}, \bar{y})$  using Matlab's `regionprops` function. This data provides the basis for quantifying the spatial patterns.

To quantify the size of a mat, we implement the radial metric of [Binder et al. \(2015\)](#), which was previously successful in quantifying the size of a filamentous yeast colony. This metric is a scaled count of the number of occupied sites at a given radial distance from the centroid. We specify three important radii using this metric. First, we define the inner radius,  $R_i$ , to be the minimum distance from the mat centroid at which we find an unoccupied site. We then define the outer radius,  $R_o$ , to be the maximum distance from the centroid at which we find an occupied site. Finally, we define the median radius,  $R_m$ , to be the maximum distance from the centroid at which greater than or equal to half of the sites are occupied. The median radius provides a suitable measure of a mat's boundary position, and hence its size. To measure the speed of mat expansion, we compute  $R_m$  for each binary image, and plot this against time in [Fig. 2.1](#). Applying a linear regression model to the mean data gives an expansion speed of  $2.54 \times 10^{-3} \text{ mm min}^{-1}$ , and the coefficient of determination  $r^2 = 0.9887$  suggests that this speed is roughly constant. We note however that there is wide variation across the experiments, and analysing all consecutive images gives expansion speeds that lie between  $1.09 \times 10^{-3} \text{ mm min}^{-1}$  and  $4.67 \times 10^{-3} \text{ mm min}^{-1}$ .

We compute an angular pair-correlation function (APCF) to quantify the spatial pattern. The APCF provides a scaled count of the angle measured from the centroid between two occupied pixels in the mat image. As we are only interested in the petals and not the mat interior, we restrict our attention to the pixels

$(x, y) \in \mathcal{D}$  such that  $R_i \leq \sqrt{(x - \bar{x})^2 + (y - \bar{y})^2} \leq R_o$ , i.e. pixels between the inner and outer radii. Due to the computational cost of calculating the APCF, we compute it from a random sample of these pixels. We then calculate the pair-correlation signal,  $F_\Theta(j)$ , using the method of [Binder et al. \(2015\)](#), and subsequently compute the discrete cosine transform of  $F_\Theta(j)$ ,

$$\hat{f}_k = \frac{2}{Nc_k} \sum_{j=0}^N \frac{F_\Theta(j)}{c_j} \cos(k\theta_j), \quad k = 0, \dots, N, \quad (2.1)$$

using  $N = 100$ . The power spectrum  $\hat{f}_k^2$  indicates the relative contribution of a floral pattern with  $k$  petals to the overall pattern. Peaks in the power spectrum therefore indicate the number of petals in a mat. We illustrate this by computing the power spectrum for experimental mat G, and present the results in [Fig. 2.2](#).

Angular pair-correlation analysis predicts a dominant mode of  $k = 8$  petals for mat G, confirming that the floral morphology develops before the end of the experiment. However, as each mat grows differently, we expect to see a range of possible modes across the experiments. Indeed, by analysing all of the images for  $t = 237$  h, we find that although modes  $k \in \{2, 3, 4\}$  are predominantly represented, there are significant peaks in the power spectra for all integer modes between  $k = 2$  and  $k = 12$  (see [Fig. A.5](#) in [Appendix A](#)). The median radius at the end of the experiment is in the range  $R_m \in [29.8, 40.3] \text{ mm}$ , with a mean of  $R_m = 37.45 \text{ mm}$ . Assuming that the experimental petal width is given by  $w = 2\pi R_m / k$ , the range of possible petal widths is  $w \in [15.6, 126.6] \text{ mm}$ . We use this data to test theoretical and numerical predictions of our mathematical model.

### 3. Mathematical model

We use a mathematical model to investigate whether nutrient-limited growth alone can explain the floral morphology observed in experiments. Unlike yeast biofilms, there is significant literature on the modelling of bacterial biofilms using both discrete and continuous models ([Dockery and Klapper, 2001; Eberl et al., 2001; Piccioreanu et al., 1998; Rahman et al., 2015; Ward and King, 2012; Ward et al., 2003](#)). Traditionally, these models describe biofilm growth on a non-reactive, impermeable substratum, whereby cells are immersed in a liquid culture medium which supplies nutrients to the biofilm. The models are commonly used to explain patterns such as fingering in the vertical direction. Past studies have

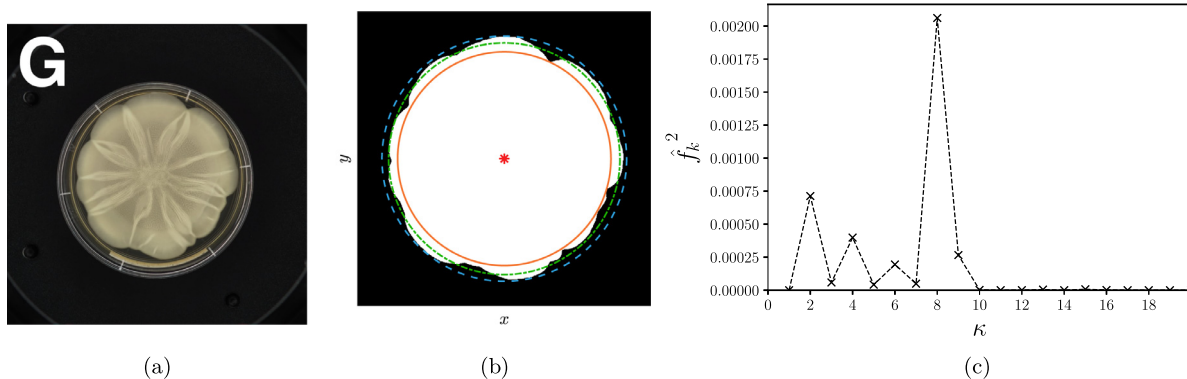


**Fig. 2.2.** Image processing results for mat G taken after ( $t = 237$  h). The number of sampled pixels is  $n = 25,000$ . (a) Mat image. (b) Processed binary image indicating the mat centroid (red asterisk), the inner radius  $R_i = 35.7$  mm (solid orange line), outer radius  $R_o = 41.0$  mm (dashed blue line), and median radius  $R_m = 38.8$  mm (dashed green line). (c) Power spectrum of the APCF. (For interpretation of the references to colour in this figure legend, the reader is referred to the web version of this article.)

shown that these patterns can depend on the nutrient uptake rate, biomass decay, or volume filling effects.

In contrast to these studies, our yeast mats receive nutrients from the substratum, which primarily restricts growth to the two-dimensional plane. As yeast cells are non-motile, mat expansion is governed by the mitosis of living cells at the mat perimeter. When starved of nutrients, yeasts have been shown to enter a stationary phase, whereby cells can begin to reproduce again if nutrient becomes available (Minois et al., 2005). In addition, unlike many bacteria, yeast does not undergo directed growth in response to nutrient gradients (Tronnolone et al., 2018). These considerations enable us to adopt simpler models than in previous studies on bacteria.

As we are interested in the effects of nutrient-limited growth alone, we neglect the extracellular matrix and interactions between cells and the substratum. As Fig. 1.1(d) shows, on low-density agar yeast mats can expand to fill an entire 90 mm Petri dish, at which time they contain approximately  $1 \times 10^{10}$  individual cells. Mats are therefore much larger than their constituent cells, so it is appropriate to model the mat in terms of continuous variables. We assume that only yeast cells and nutrients are present on the Petri dish, and define  $n(\vec{x}, t)$  to be the yeast cell density, and  $g(\vec{x}, t)$  to be the nutrient (glucose) concentration.

Reaction-diffusion equations provide a simple framework to describe the features of nutrient-limited growth. Reaction-diffusion systems have been used extensively as prototype models in studies on pattern formation since the pioneering work of Turing (1952). Such models also commonly admit travelling wave solutions in which fronts advance at a constant speed (Grindrod, 1991), which matches our experimental observations. Specifically for yeast colonies, a useful basis is the Gray-Kirwan model (Edelstein-Keshet, 1988; Gray and Kirwan, 1974), which was the first use of a reaction-diffusion system to model yeast growth. In one spatial dimension, their model is

$$\frac{\partial n}{\partial t} = D_n \frac{\partial^2 n}{\partial x^2} + png, \quad (3.1a)$$

$$\frac{\partial g}{\partial t} = D_g \frac{\partial^2 g}{\partial x^2} - cpng, \quad (3.1b)$$

where  $D_n$  and  $D_g$  are the diffusion coefficients for yeast cells and glucose respectively,  $p$  is the cell proliferation rate, i.e. the rate of increase in colony area per unit of nutrient, and  $c$  is the quantity of glucose consumed per new cell.

However, experimental mats expand by growth of new cells at the perimeter, and not by traditional Fickian diffusion. To account for this, a more suitable model would incorporate a non-linear diffusion term for cell spread, whereby the rate of spread is directly proportional to the local cell density. Similar systems have

been previously proposed by Chen et al. (2014) (for yeast), and Kawasaki et al. (1997) (for bacteria). However, as yeast cannot grow in response to nutrient gradients, we expect that the cell spread term will depend only on the cell density  $n$ . A simple reaction-diffusion system that captures this behaviour is

$$\frac{\partial n}{\partial t} = D_n \nabla \cdot (n \nabla n) + png, \quad (3.2a)$$

$$\frac{\partial g}{\partial t} = D_g \nabla^2 g - cpng. \quad (3.2b)$$

This non-linear diffusion model has been shown to produce compactly supported solutions whereby cell density is only non-zero in a finite envelope (Müller and van Saarloos, 2002), unlike the Gray-Kirwan model (Billingham and Needham, 1991). The system (3.2) is therefore more suitable for modelling finite-sized experimental mats, for which we need to track the boundary position. We investigate this model for the remainder of the article.

### 3.1. Non-dimensionalisation and scaling

To non-dimensionalise the model, we introduce the dimensionless variables

$$\hat{t} = \mathcal{G}pt, \quad \hat{x}_i = \sqrt{\frac{\mathcal{G}p}{D_g}} x_i, \quad \hat{n}(\vec{\hat{x}}, \hat{t}) = \frac{n(\vec{x}, t)}{\mathcal{N}}, \text{ and } \hat{g}(\vec{\hat{x}}, \hat{t}) = \frac{g(\vec{x}, t)}{\mathcal{G}}, \quad (3.3)$$

where  $\mathcal{N}$  is the measured mean final cell density, and  $\mathcal{G}$  is the initial glucose concentration. In terms of these new dimensionless variables (3.3), the model (3.2) becomes (dropping carets)

$$\frac{\partial n}{\partial \hat{t}} = D \nabla \cdot (n \nabla n) + ng, \quad (3.4a)$$

$$\frac{\partial g}{\partial \hat{t}} = \nabla^2 g - \Upsilon ng. \quad (3.4b)$$

In writing (3.4), we have introduced the dimensionless parameters

$$D = \frac{\tilde{D}_n}{D_g}, \quad \text{and} \quad \Upsilon = \frac{c\mathcal{N}}{\mathcal{G}}, \quad (3.5)$$

where  $\tilde{D}_n = \mathcal{N}D_n$  is the effective cell diffusion coefficient.

As this analysis shows, to scale the model to experimental data, we need estimates for  $D_g$ ,  $\mathcal{N}$ ,  $\mathcal{G}$ ,  $p$ ,  $c$ , and  $D_n$ . We use the empirical relationship of Slade et al. (1966) to estimate  $D_g$ , and we can estimate each of  $\mathcal{N}$ ,  $\mathcal{G}$ , and  $p$ , directly from experimental data. To estimate  $c$ , we assume that  $\Upsilon = 1$ , i.e. that all of the consumed nutrient is involved in the generation of new cells, and that all of the

**Table 3.1**  
Experimental values for relevant dimensional parameters.

Parameter	Value	Units	Source
$D_g$	4.01e-2	$\text{mm}^2 \text{ min}^{-1}$	Slade et al. (1966), Longsworth (1955)
$\mathcal{G}$	9.24e-5	$\text{g mm}^{-2}$	Experimental design
$N$	3.34e6	$\text{cells mm}^{-2}$	Mat images
$p$	15.28	$\text{mm}^2 \text{ g}^{-1} \text{ min}^{-1}$	Experimental data
$c$	2.77e-11	$\text{g cell}^{-1}$	Assumption

nutrient is consumed by the end of the experiment. Our parameter estimates are listed in Table 1. Further details on how each is calculated are provided in Appendix B.

Knowledge of  $D_g$ ,  $p$ , and  $\mathcal{G}$  is sufficient to determine the experimental length and time scales. Using (3.3), the time scale is  $\hat{t} = (1.412 \times 10^{-3})t$ , for  $t$  in minutes, and the radial length scale is  $\hat{r} = 0.1933r$ , for  $r$  given in millimetres. Given that we estimate the mat to expand at a constant speed of  $2.54 \times 10^{-3} \text{ mm min}^{-1}$ , this gives a mean dimensionless expansion speed of  $v = 0.348$ , while all results lie within the range  $v \in [0.150, 0.639]$ . The median radii at the end of the experiment corresponds to a dimensionless radius of  $\hat{r} \in [5.71, 7.54]$ , with a mean of  $\hat{r} = 7.02$ , and the dimensionless range of possible petal widths is  $\hat{w} \in [2.99, 23.68]$ . We use these dimensionless quantities when comparing the model and experiments.

In Section 4, we exploit the finding that mats appear to expand at a constant radial speed by constructing travelling wave solutions to the model (3.4). We apply geometric singular perturbation theory to prove the existence of such solutions for  $D = 0$ , and provide an analytical approximation of the slow manifold on which dynamics for small  $D$  occur. We then exploit the fact that sharp-fronted solutions are only possible for a unique minimum speed to estimate the diffusion ratio  $D$ .

#### 4. Travelling wave solutions

A travelling wave solution to a partial differential equation is a solution that advances at a constant speed while retaining its shape. Previous studies have used travelling wave solutions to estimate parameters in experiments containing cell density fronts that advance at a constant speed (Johnston et al., 2014; Maini et al., 2004), similar to those observed in our experiments. We seek a travelling wave solution to (3.4) that is valid for large mats. To do so, we write the model in polar co-ordinates, and following Gallegos et al. (2006) assume that  $r \gg 1$ , which yields the system

$$\frac{\partial n}{\partial t} = D \frac{\partial}{\partial r} \left( n \frac{\partial n}{\partial r} \right) + ng, \quad (4.1a)$$

$$\frac{\partial g}{\partial t} = \frac{\partial^2 g}{\partial r^2} - ng. \quad (4.1b)$$

To search for a travelling wave solution to (4.1), we make the ansatz that solutions advance radially at constant speed. To facilitate this, we introduce the Galilean co-ordinate  $z = r - vt \in (-\infty, \infty)$ , where  $v > 0$  is the constant wave speed. This yields the ordinary differential equations,

$$D \frac{d}{dz} \left( n \frac{dn}{dz} \right) + v \frac{dn}{dz} + ng = 0, \quad (4.2a)$$

$$\frac{d^2 g}{dz^2} + v \frac{dg}{dz} - ng = 0. \quad (4.2b)$$

The yeast cell density is zero in the far-field, and we assume that the far-field glucose concentration remains constant at the initial level. We also assume that the experiment continues until the glucose concentration is zero, at which point the yeast cell density

remains constant. The boundary conditions associated with the dimensionless system (4.2) are therefore

$$\lim_{z \rightarrow \infty} n(z) = 0, \quad \lim_{z \rightarrow -\infty} n(z) = 1, \quad \lim_{z \rightarrow \infty} g(z) = 1, \quad \text{and} \quad \lim_{z \rightarrow -\infty} g(z) = 0, \quad (4.3)$$

with all derivatives of  $n$  and  $g$  with respect to  $z$  vanishing as  $z \rightarrow \pm \infty$ . Now, if we add (4.2a) and (4.2b), integrate once with respect to  $z$ , and apply the boundary conditions (4.3), we obtain the conserved quantity

$$Dn \frac{dn}{dz} + vn + \frac{dg}{dz} + vg = v. \quad (4.4)$$

To construct the travelling wave solution, it is convenient to introduce the new variables

$$u(z) = n \frac{dn}{dz}, \quad \text{and} \quad w(z) = \frac{dg}{dz}, \quad (4.5)$$

whereby

$$\lim_{z \rightarrow -\infty} u(z) = \lim_{z \rightarrow \infty} u(z) = 0, \quad \text{and} \quad \lim_{z \rightarrow -\infty} w(z) = \lim_{z \rightarrow \infty} w(z) = 0. \quad (4.6)$$

Using these variables, we write (4.2) as the four-dimensional dynamical system

$$n \frac{dn}{dz} = u, \quad (4.7a)$$

$$\frac{dg}{dz} = w, \quad (4.7b)$$

$$D \frac{du}{dz} = -\frac{vu}{n} - ng, \quad (4.7c)$$

$$\frac{dw}{dz} = ng - vw. \quad (4.7d)$$

Owing to the conserved quantity (4.4), there is a three-dimensional invariant surface on which the dynamics of (4.7) occur. Replacing the variable  $u$  with (4.4) allows us to reduce (4.7) to the three-dimensional system,

$$n \frac{dn}{dz} = \frac{1}{D} (v - vn - w - vg), \quad (4.8a)$$

$$\frac{dg}{dz} = w, \quad (4.8b)$$

$$\frac{dw}{dz} = ng - vw. \quad (4.8c)$$

Finally, we use the technique first proposed by Aronson (1980) to remove the singularity as  $n \rightarrow 0$  in (4.8a), while still giving a system that is topologically equivalent to (4.8). In our problem, this involves introducing a new independent variable  $\zeta$  defined as

$$\frac{d\zeta}{dz} = n^{-1} \Rightarrow \zeta = \int_0^z n^{-1} ds, \quad (4.9)$$

and re-writing the variables as

$$N(\zeta) = n(z), \quad G(\zeta) = g(z), \quad \text{and} \quad W(\zeta) = w(z). \quad (4.10)$$

In terms of the new variables (4.10), the three-dimensional system becomes

$$\frac{dN}{d\zeta} = \frac{1}{D}(v - vN - W - vG), \quad (4.11a)$$

$$\frac{dG}{d\zeta} = WN, \quad (4.11b)$$

$$\frac{dW}{d\zeta} = N^2G - vWN. \quad (4.11c)$$

A travelling wave solution to the model (4.1) exists if there is a heteroclinic connection between the equilibria  $(N, G, W) = (1, 0, 0)$  and  $(0, 1, 0)$ , which correspond to the boundary conditions as  $z \rightarrow -\infty$  and  $z \rightarrow \infty$ , respectively. We therefore use the system (4.11) to investigate the existence of such solutions. In doing so, we employ geometric singular perturbation theory to exploit the singular limit as  $D \rightarrow 0$ .

#### 4.1. Dynamics for small D

We anticipate that glucose diffusion will occur much faster than the spread of yeast cells. As a result, we expect that  $\mathcal{N}D_n = \tilde{D}_n \ll D_g$ . It is therefore appropriate to consider the behaviour of the dynamical system (4.11) for small diffusion ratio, which we facilitate by letting  $0 < D = \epsilon \ll 1$ . This allows us to recast (4.11) as a slow-fast system, which provides a framework for which to investigate the existence of travelling wave solutions (Balasuriya et al., 2007; Harley et al., 2014; Marchant et al., 2001). Introducing the small parameter, we can re-write the system (4.11) as

$$\epsilon \frac{dN}{d\zeta} = v - vN - W - vG, \quad (4.12a)$$

$$\frac{dG}{d\zeta} = WN, \quad (4.12b)$$

$$\frac{dW}{d\zeta} = N^2G - vWN, \quad (4.12c)$$

and we refer to this as the *slow subsystem*. If we then introduce a new independent variable  $\gamma = \zeta/\epsilon$ , we can rewrite (4.12) as the *fast subsystem*,

$$\frac{dN}{d\gamma} = v - vN - W - vG, \quad (4.13a)$$

$$\frac{dG}{d\gamma} = \epsilon WN, \quad (4.13b)$$

$$\frac{dW}{d\gamma} = \epsilon(N^2G - vWN). \quad (4.13c)$$

An advantage of formulating the problem as a slow-fast system is that taking the singular limit in either subsystem yields a regular problem of lower dimension than the full system. For example, if we take the limit as  $\epsilon \rightarrow 0$  in the slow subsystem (4.12), we obtain a two-dimensional problem with an algebraic constraint,

$$0 = v - vN - W - vG, \quad (4.14a)$$

$$\frac{dG}{d\zeta} = WN, \quad (4.14b)$$

$$\frac{dW}{d\zeta} = N^2G - vWN. \quad (4.14c)$$

We refer to the system (4.14) as the *reduced problem*. Similarly, taking the limit as  $\epsilon \rightarrow 0$  in the fast subsystem yields a one-dimensional problem with two parameters,

$$\frac{dN}{d\gamma} = v - vN - W - vG, \quad (4.15a)$$

$$\frac{dG}{d\gamma} = 0, \quad (4.15b)$$

$$\frac{dW}{d\gamma} = 0, \quad (4.15c)$$

which we refer to as the *layer problem*.

Using geometric singular perturbation theory (Fenichel, 1979), we analyse the reduced and layer problems (4.14) and (4.15) independently to investigate the existence of solutions to the full system (4.11). In doing so, we verify the theoretical result that there is an invariant surface on which the dynamics of the full system occur for non-zero  $\epsilon$ , and prove the existence of travelling wave solutions for  $\epsilon = 0$ .

#### 4.1.1. Layer problem

We begin the analysis by considering the layer problem. In the system (4.15), the plane  $S_0 : v - vN - W - vG = 0$  consists entirely of fixed points, and is the centre manifold of these equilibria. We refer to  $S_0$  as the *critical manifold*. For  $\epsilon = 0$ , solution trajectories of the full system are attracted exponentially quickly to  $S_0$  along lines of constant  $G$  and  $W$ , as governed by the layer problem (4.15). As the equation for  $S_0$  is also the algebraic constraint (4.14a), the dynamics of the reduced problem (4.14) are confined to this critical manifold. According to geometric singular perturbation theory, when  $\epsilon$  is small but non-zero, the dynamics of the full system (4.12, 4.13) will occur on an invariant curved entity  $\mathcal{O}(\epsilon)$  away from  $S_0$  (Jones, 1995). We refer to  $S_\epsilon$  as the *slow manifold*.

We can approximate the shape of  $S_\epsilon$  analytically by considering the dynamics of the fast subsystem (4.13). Assuming that  $S_\epsilon$  is an invariant surface  $\mathcal{O}(\epsilon)$  away from  $S_0$ , we can write

$$S_\epsilon : N = 1 - G - \frac{W}{v} + \epsilon f(G, W) + \mathcal{O}(\epsilon^2), \quad (4.16)$$

for some function  $f$ . Differentiating this with respect to the fast variable  $\gamma$ , we obtain

$$\frac{dN}{d\gamma} = -\frac{dG}{d\gamma} - \frac{1}{v} \frac{dW}{d\gamma} + \epsilon \left( \frac{\partial f}{\partial G} \frac{dG}{d\gamma} + \frac{\partial f}{\partial W} \frac{dW}{d\gamma} \right) + \mathcal{O}(\epsilon^2). \quad (4.17)$$

Substituting relevant terms from the fast subsystem (4.13), we obtain

$$S_\epsilon : W_\epsilon = v(1 - N - G) + \epsilon \frac{N^2G}{v} + \mathcal{O}(\epsilon^2), \quad (4.18)$$

which is an asymptotic approximation to the shape of the slow manifold as  $\epsilon \rightarrow 0$ . As expected, the equation for  $S_\epsilon$  (4.18) gives the critical manifold  $S_0$  at  $\mathcal{O}(1)$ .

Knowledge of the shape of  $S_\epsilon$  enables us to estimate the paths taken by trajectories for  $\epsilon \neq 0$ . To test this, we neglect  $\mathcal{O}(\epsilon^2)$  terms and compute the slow manifold  $S_\epsilon$  numerically. To compare this surface with solution trajectories, we integrate the fast subsystem (4.13) numerically using a fourth-order Runge–Kutta scheme, with  $N_\gamma = 25,000$  points, and  $\Delta\gamma = 1$ . As there is a one-dimensional unstable manifold associated with the equilibrium  $(1, 0, 0)$ , we take our initial condition to be a small distance from this point in the unstable direction. An example of these computations is shown in

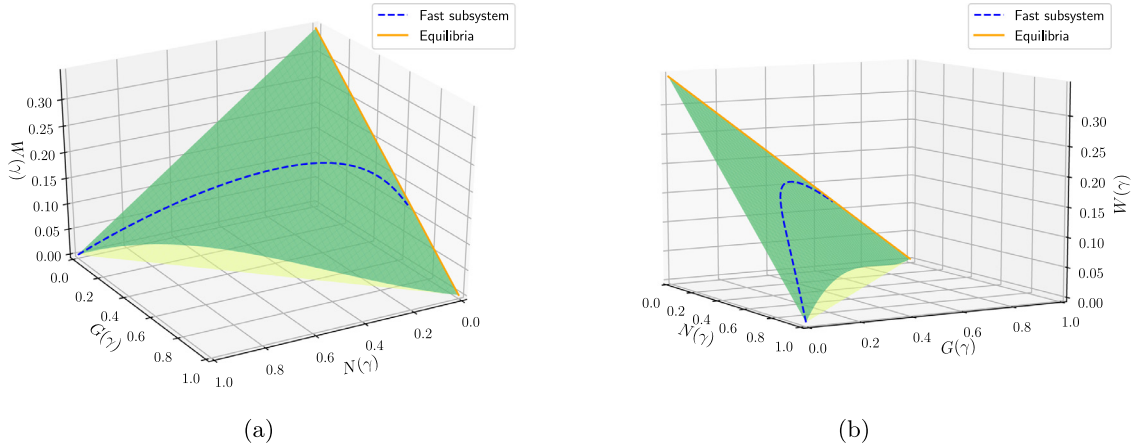


**Fig. 4.1.** Two views of the critical manifold  $S_0$  (yellow), and approximate slow manifold  $S_\epsilon$  (green), for  $v = 0.348$ , and  $\epsilon = 0.1$ . A trajectory of the numerical solution to the fast subsystem (4.13) is shown with the dashed blue line, and the equilibria of (4.13) are shown in orange. (For interpretation of the references to colour in this figure legend, the reader is referred to the web version of this article.)

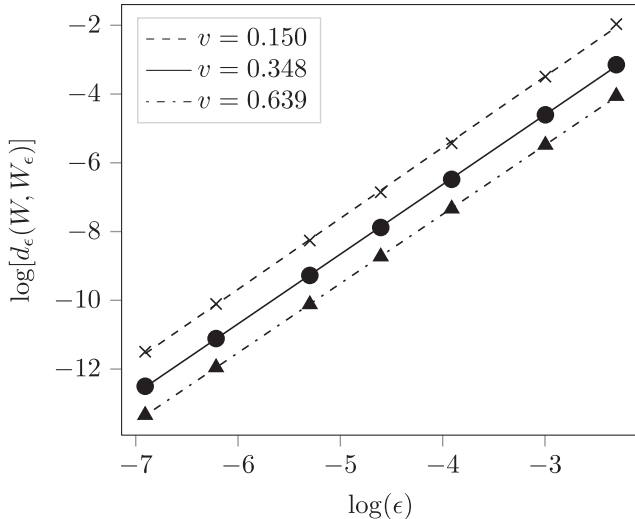


**Fig. 4.2.** A logarithmic plot of  $d_\epsilon(W, W_\epsilon)$  for  $\epsilon \in [0.001, 0.1]$ , computed for the biologically relevant wave speeds  $v \in \{0.150, 0.348, 0.639\}$ .

Fig. 4.1, where as predicted the fast subsystem trajectory closely follows the slow manifold.

To test the accuracy of our formula (4.18), we compute the metric

$$d_\epsilon(W, W_\epsilon) = \sqrt{\sum_{i=1}^{N_y} (W - W_\epsilon)_i^2}, \quad (4.19)$$

which is the  $L^2$ -norm of the vector of distances between points along the fast subsystem trajectory  $(N, G, W)_i$ , and the slow manifold  $(N, G, W_\epsilon)_i$ , for  $i = 1, \dots, N_y$ . We compute this quantity for the minimum, mean, and maximum wave speeds, and plot the results in Fig. 4.2. As the presented data follows straight lines on a logarithmic scale, we deduce that  $d_\epsilon(W, W_\epsilon) \sim \mathcal{O}(\epsilon^m)$ , where  $m$  is the slope of the graph. For the minimum, mean, and maximum wave speeds, we find  $m = 2.06$ ,  $m = 2.03$ , and  $m = 2.01$ , respectively, which verifies the slow manifold approximation (4.18). As predicted by the theory, this justifies the existence of an invariant slow manifold on which the dynamics of (4.12) and (4.13) occur for non-zero  $\epsilon$ . We combine this result with analysis of the reduced problem to investigate the existence of travelling wave solutions to the full system (4.11).

#### 4.1.2. Reduced problem

Unlike the layer problem, the reduced problem (4.14) contains an algebraic constraint in addition to differential equations. Due to this algebraic constraint (4.14a), we can rewrite the reduced problem (4.14) as the two-dimensional system

$$\frac{dG}{d\zeta} = W \left( 1 - \frac{W}{v} - G \right), \quad (4.20a)$$

$$\frac{dW}{d\zeta} = \left( 1 - \frac{W}{v} - G \right)^2 G - vW \left( 1 - \frac{W}{v} - G \right). \quad (4.20b)$$

A heteroclinic connection between  $(1, 0, 0)$  and  $(0, 1, 0)$  in the full system (4.11) corresponds to a heteroclinic connection between  $(G, W) = (0, 0)$  and  $(1, 0)$  in the two-dimensional reduced system (4.20). To investigate the dynamics away from the line  $1 - W/v - G = 0$ , we perform a second co-ordinate transformation,

$$\frac{d\tilde{\zeta}}{d\zeta} = 1 - \frac{W}{v} - G \Rightarrow \tilde{\zeta} = \int_0^\zeta \left( 1 - \frac{W}{v} - G \right) ds, \quad (4.21)$$

which yields the system

$$\frac{dG}{d\tilde{\zeta}} = W, \quad (4.22a)$$

$$\frac{dW}{d\tilde{\zeta}} = \left( 1 - \frac{W}{v} - G \right) G - vW. \quad (4.22b)$$

Linearising about the fixed points of (4.22), we find that for any  $v > 0$  the point  $(0, 0)$  has a one-dimensional unstable manifold in the direction  $(v/2 + \sqrt{v^2 + 4}/2, 1)$ , and that  $(1, 0)$  is a stable node. Furthermore, a trajectory leaving  $(0, 0)$  along the unstable direction is confined to the forward-invariant triangular region

$$\{(G, W) \mid 0 \leq G \leq 1, 0 \leq W \leq v(1 - G)\}, \quad (4.23)$$

as we notice that flow on the boundaries of this region is never in the outward direction. Therefore, as  $(0, 0)$  and  $(1, 0)$  are the only two equilibria of (4.22), the Poincaré-Bendixson theorem guarantees that the equilibrium  $(1, 0)$  is the  $\omega$ -limit set of a trajectory emanating from  $(0, 0)$  (Alligood et al., 1996). This proves that a heteroclinic connection between  $(0, 0)$  and  $(1, 0)$  exists for the system (4.22), and therefore that travelling wave solutions to the full system (4.11) exist for  $D = 0$ .

However, if  $W > v(1 - G)$ , the transformation (4.21) scales the independent variable negatively. Therefore, when  $W > v(1 - G)$ , flow of the reduced problem (4.20) is in the opposite direction

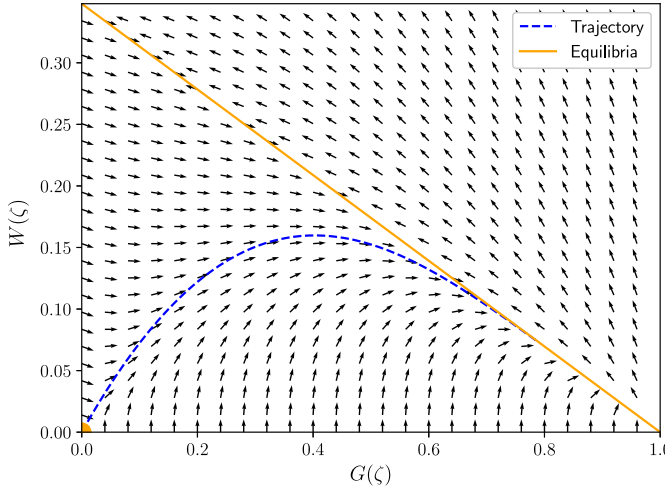


**Fig. 4.3.** Direction field of the reduced problem (4.20) with  $v = 0.348$  (black arrows). The equilibria, including the line  $W = v(1 - G)$  and the point  $(0, 0)$  are shown in orange, and the dashed blue line is a trajectory computed numerically. (For interpretation of the references to colour in this figure legend, the reader is referred to the web version of this article.)

to (4.22). A heteroclinic connection between  $(0, 0)$  and  $(1, 0)$  in the reduced problem (4.20) is therefore impossible if the trajectory enters the region  $W > v(1 - G)$ , as Fig. 4.3 illustrates. Although flow along the critical manifold always remains in the region  $W \leq v(1 - G)$ , the slow manifold approximation (4.18) is only accurate to  $\mathcal{O}(\epsilon^2)$  as  $\epsilon \rightarrow 0$ . It may be possible for a trajectory of the full system to intersect the  $(G, W)$  plane such that  $W > v(1 - G)$ , in which case Fig. 4.3 suggests that no biologically relevant travelling wave solution is possible. Numerically integrating (4.11) allows us to determine whether this occurs, giving results that enable us to estimate the diffusion ratio.

#### 4.2. Estimating the diffusion ratio

Solving the full system numerically allows us to explore the existence of travelling wave solutions in the biologically relevant  $D \neq 0$  regime. Integrating (4.11), also using a fourth-order Runge-Kutta scheme, for constant  $D$  we observe three different types of qualitative behaviour depending on  $v$ . First, if the wave speed is sufficiently small, the solution trajectory intersects the  $(G, W)$  plane at a point  $(G_i, W_i)$  such that  $\delta := W_i - v(1 - G_i) > 0$ . However, as we continuously increase the wave speed,  $\delta$  decreases and eventually reaches zero. If we increase  $v$  further, the trajectory intersects the  $(G, W)$  plane at the equilibrium  $(N, G, W) = (0, 1, 0)$ . These possibilities are illustrated for  $D = 0.47$  in Fig. 4.4, and the corresponding travelling wave profiles are given in Fig. 4.5.

The wave speed  $v = 0.25$  is such that  $\delta > 0$ . As the reduced problem direction field predicts, no biologically relevant travelling wave solution exists. Fig. 4.5(a), in which  $N(\zeta)$  and  $G(\zeta)$  become negative, illustrates this. In contrast, for  $v = 0.5$  the trajectory eventually enters  $(1, 0, 0)$ , giving rise to the biologically valid travelling wave solution in Fig. 4.5(c). The minimum wave speed that gives a valid travelling wave solution is  $v = 0.348$ , in which case the solution trajectory reaches an equilibrium along the line  $W = v(1 - G)$ , such that  $N(\zeta) = 0$  and  $G(\zeta) \neq 1$ . This corresponds to the  $z < 0$  region of the solution to (4.8) found by Müller and van Saarloos (2002), who used a shooting argument to numerically demonstrate the existence of sharp-fronted travelling wave solutions in one dimension. As part of their analysis, they also found that the minimum wave speed  $v_{min}(D)$  is unique, and depends only on  $D$ . If we compute solutions to the one-dimensional model (4.1) with arbitrary initial conditions, we find that a sharp-

fronted profile emerges and propagates at  $v_{min}$ . Due to this, we adopt  $v_{min}$  as the experimental mat expansion speed. In doing so, we can determine the effect of  $D$  on the speed of mat expansion.

As Fig. 4.6 shows, there is a monotonic relationship between the diffusion ratio and the minimum wave speed. Observing the expansion speed in an experiment therefore allows us to uniquely infer the diffusion ratio. In Section 3.1, we found a mean experimental expansion speed of  $v = 0.348$ , and that across all experiments the expansion speed lay within the range  $v \in [0.150, 0.639]$ . Computing travelling wave solutions numerically, we find these values correspond to a mean diffusion ratio of  $D = 0.470$ , and that the experimental range is  $D \in [0.181, 1.02]$ . This completes our parameterisation of the model, allowing us to proceed to predicting two-dimensional floral pattern formation.

#### 5. Predicting two-dimensional floral pattern formation

So far, we have used the fact that a mat expands at a roughly constant speed to parameterise the model. We now switch our attention to investigating whether the model can predict the floral morphology. In experiments, there are small deviations to the mat shape, cell density, and nutrient concentration as cells grow and consume nutrient. We investigate whether these small perturbations can grow into a floral pattern, driven only by nutrient-limited growth. To do this, we use a combination of linear stability analysis and numerical solutions to the model.

##### 5.1. Linear stability analysis

To investigate pattern formation in a large circular mat with negligible perimeter curvature, we consider the model in two dimensional Cartesian co-ordinates,

$$\frac{\partial n}{\partial t} = D \left[ \frac{\partial}{\partial x} \left( n \frac{\partial n}{\partial x} \right) + \frac{\partial}{\partial y} \left( n \frac{\partial n}{\partial y} \right) \right] + ng, \quad (5.1a)$$

$$\frac{\partial g}{\partial t} = \frac{\partial^2 g}{\partial x^2} + \frac{\partial^2 g}{\partial y^2} - ng. \quad (5.1b)$$

Essentially, this introduces the  $y$  co-ordinate normal to the radial direction in the one-dimensional model (4.1) considered in Section 4. To account for perturbations in the mat shape, we introduce the co-ordinate transformation

$$\xi = x - vt + \varepsilon e^{iqy+\omega t}, \quad \eta = y, \quad \tau = t, \quad (5.2)$$

where  $0 < \varepsilon \ll 1$  is the small amplitude of perturbations,  $q > 0$  is the perturbation wave number, and  $\omega$  is the growth rate (Horváth et al., 1993; Sivashinsky, 1977). The new independent variable,  $\xi$ , is a co-ordinate that follows the perturbed wave front as it advances. To account for variations in the cell density and nutrient concentration, we expand the cell density and nutrient concentration as

$$n(\xi, \eta, \tau) = n_0(\xi) + \varepsilon n_1(\xi) e^{iq\eta+\omega\tau} + \mathcal{O}(\varepsilon^2), \quad (5.3a)$$

$$g(\xi, \eta, \tau) = g_0(\xi) + \varepsilon g_1(\xi) e^{iq\eta+\omega\tau} + \mathcal{O}(\varepsilon^2), \quad (5.3b)$$

as  $\varepsilon \rightarrow 0$ . Substituting (5.3) into the partial differential equations (5.1), at  $\mathcal{O}(1)$  we recover the travelling wave equations (4.2) for  $n_0(\xi)$  and  $g_0(\xi)$ . Linearising about these solutions yields a spectral problem at  $\mathcal{O}(\varepsilon)$ , consisting of two second-order ordinary differential equations. Solving this problem for the first-order correction functions  $n_1(\xi)$  and  $g_1(\xi)$  enables us to investigate the spectral stability of planar travelling wave solutions to (5.1). Specifically, we are interested in finding instabilities, whereby an eigenvalue of the spectral problem has positive real part. Since the spectral problem is posed on an infinite-dimensional space, we also consider dispersion relations that locate the essential, or continuous spectrum.

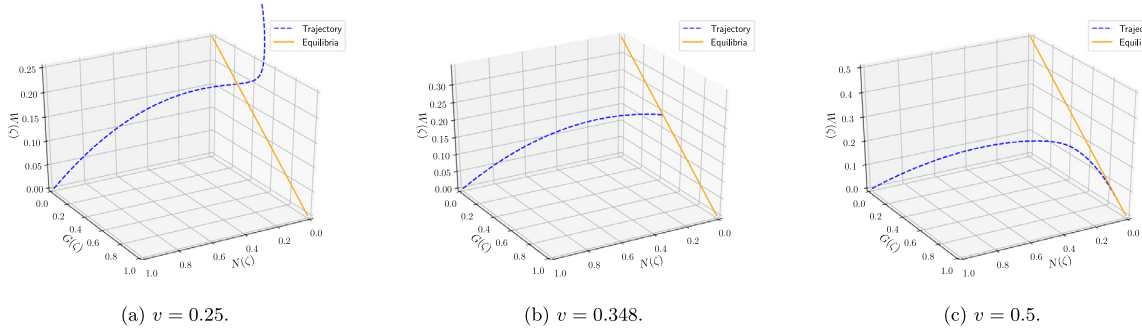


**Fig. 4.4.** Numerical solutions of the full dynamical system (4.11) for  $D = 0.47$  and different  $v$ .

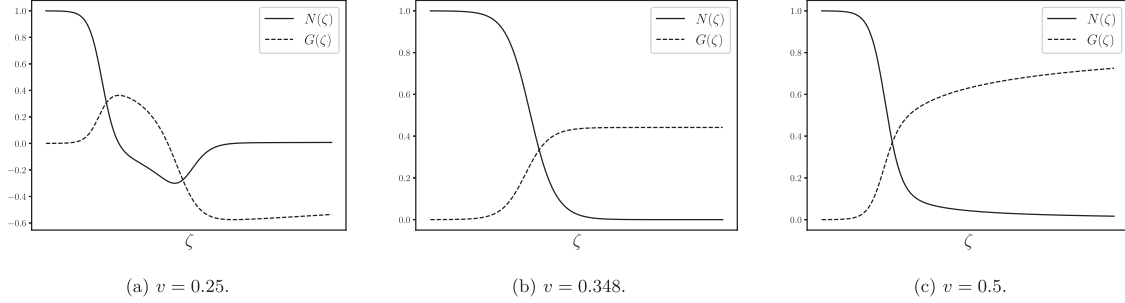


**Fig. 4.5.** Travelling wave profiles for  $D = 0.47$  and different  $v$ .

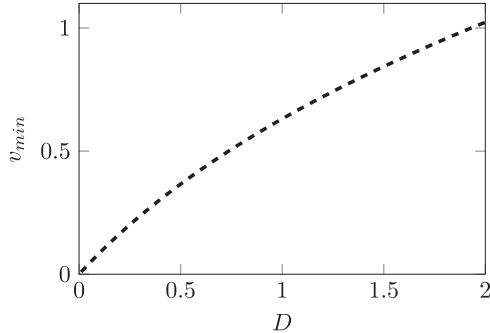


**Fig. 4.6.** Effect of the diffusion ratio on the speed at which a large yeast mat biofilm expands.

We refer the reader to Kapitula and Promislow (2013) for further details. For the model (5.1), Müller and van Saarloos (2002) compute the dispersion relations using a numerical shooting method. In doing so, they show that for a given  $D$ , there is a unique growth rate  $\omega(D, q)$  that corresponds to each wave number  $q$ . We compute these dispersion curves for the minimum, maximum, and mean  $D$  predicted by the experimental data in Fig. 5.1.

A travelling wave solution is linearly stable to all perturbations with wave numbers that give  $\omega < 0$ , and linearly unstable to perturbations with wave numbers that give  $\omega > 0$ . Fig. 5.1 shows that there is a range of wave numbers for which the travelling wave solution is linearly unstable for all experimentally feasible values of  $D$ . For example, for  $D = 0.47$ , we observe instability for  $q \in (0, 0.672)$ . Owing to the sinusoidal form of the perturbations (5.3), the characteristic petal width is given by  $\hat{w} = 2\pi/q$ . Therefore, for  $D = 0.47$  we could theoretically observe petals with any width  $\hat{w} > 9.35$ . This overlaps the feasible experimental range  $\hat{w} \in [2.99, 23.68]$ , which suggests that the combination of nutrient-limited cell proliferation and non-linear diffusion is a potential mechanism for floral pattern formation.

In addition, we expect the wave number corresponding to the fastest growth rate  $\omega$  to eventually dominate the experimental pattern. The dispersion curves of Fig. 5.1 therefore allow us to predict the number of petals in an experimental mat. The most unstable wave numbers for  $D = 0.181$ ,  $D = 0.47$ , and  $D = 1.02$  are  $q = 0.420$ ,  $q = 0.358$ , and  $q = 0.232$ , respectively. Using the mean final radius  $\hat{r} = 7.02$ , the predicted number of petals is given by  $\kappa = q\hat{r}$ . The most unstable wave number range therefore corresponds to  $\kappa \in \{2, 3\}$ , which agrees well with the dominant modes of experimental images (see Fig. A.5 in Appendix A). However, the linear stability analysis presented here is only valid for large mats with negligible curvature, and for short times after the onset of instability. Previous studies have shown that curvature can have a significant effect on the wave speed (Francisco Leyva et al., 2013; Hilhorst et al., 2008). Therefore, to investigate pattern evolution beyond the linear regime, and in finite-sized circular mats, we compute numerical solutions to the partial differential equations (5.1).

## 5.2. Two-dimensional numerical solutions

In this section, we compute numerical solutions to the two-dimensional model (5.1). Our numerical scheme incorporates second-order accurate finite differences for spatial derivatives, and a Crank–Nicolson scheme for time integration. At each time step, we solve the resulting linear system iteratively using the generalised minimal residual (GMRES) method (Saad and Schultz, 1986). Based on a grid convergence study, we find that a grid spacing of  $\Delta x = \Delta y = 0.1$ , and time step size of  $\Delta t = 0.001$  produces accurate solutions that are independent of both grid spacing and time step size. We employ these in all of our numerical solutions. For full details of the numerical scheme and convergence tests, see Appendix C.

We first use our numerical method to validate the linear stability analysis of Müller and van Saarloos (2002). This allows us to resolve an apparent discrepancy in the numerical solutions of Kitsunezaki (1997), who tested two theoretically unstable cases using a discrete model, but only observed the instability in one case.

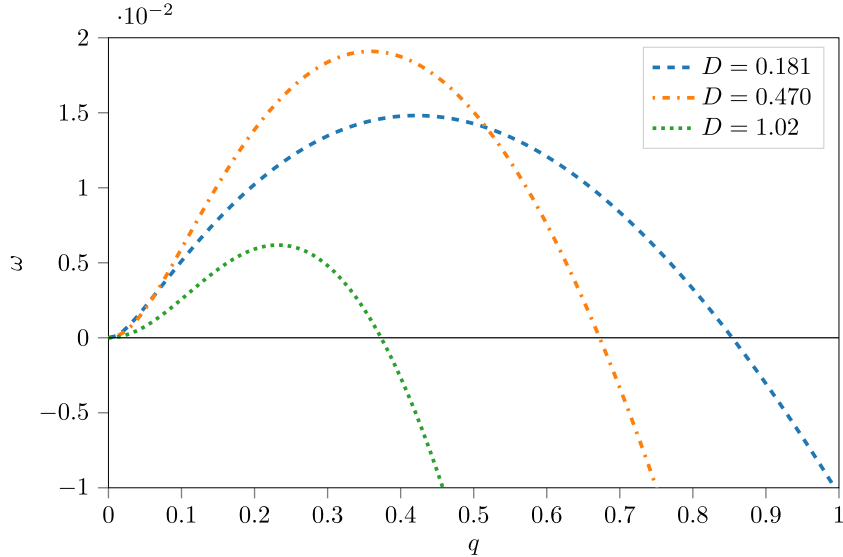


**Fig. 5.1.** Dispersion curves showing the dependence of the growth rate  $\omega$  on the wave number  $q$  and diffusion ratio  $D$ , for three experimentally feasible values of  $D$ .

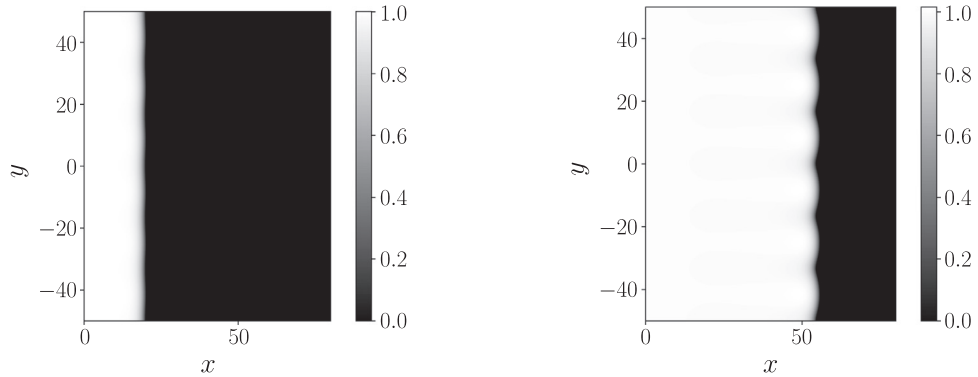


**Fig. 5.2.** Numerical cell density solutions  $n(x, y, t)$  to the two-dimensional model (5.1), showing the predicted instability. Solutions computed using the ansatz (5.4) for the initial condition, and parameter values  $D = 0.470$ ,  $q = 0.3770$ , and  $\varepsilon = 0.1$ .

To compute our solutions, we omit  $\mathcal{O}(\varepsilon^2)$  terms and impose perturbations of the form

$$n(\xi, y, t) = n_0(\xi) + \varepsilon n_1(\xi) \cos(qy) e^{\omega t}, \quad (5.4a)$$

$$g(\xi, y, t) = g_0(\xi) + \varepsilon g_1(\xi) \cos(qy) e^{\omega t}. \quad (5.4b)$$

The functions  $n_0(\xi)$  and  $g_0(\xi)$  are the travelling wave solutions, and  $n_1(\xi)$  and  $g_1(\xi)$  are the first-order correction functions, both of which we have computed. Using (5.4a), we obtain

$$\omega t = \log \left[ 1 + \frac{n(\xi, y, t) - n(\xi, y, 0)}{\varepsilon n_1(\xi) \cos(qy)} \right], \quad (5.5)$$

which we can use to compute the growth rate  $\omega$  in numerical results.

We compute the dispersion relation numerically for the mean experimental value of  $D = 0.470$ . To do so, we solve (5.1) numerically, and compute the quantity (5.5) for  $t \in [0, 100]$  in increments of ten. We then employ least squares linear fitting to obtain an estimate for the growth rate  $\omega(D, q)$ , and repeat this process for five theoretically unstable wave numbers. In each case, our numerical method reproduces the predicted instability, an example of which is shown in Fig. 5.2. In addition, the growth rate predictions show good agreement with the theory, as illustrated in Fig. 5.3. These results validate the linear stability analysis of Müller and van Saarloos (2002).

In addition to validating the linear stability analysis for planar fronts, we are also interested in whether the model captures petal formation in the circular geometry relevant to yeast colony growth. To investigate this, we compute solutions using a perturbed circular front as the initial condition. We impose perturbations of the form

$$\xi_r = r - vt + \varepsilon f_p(\theta), \quad (5.6a)$$

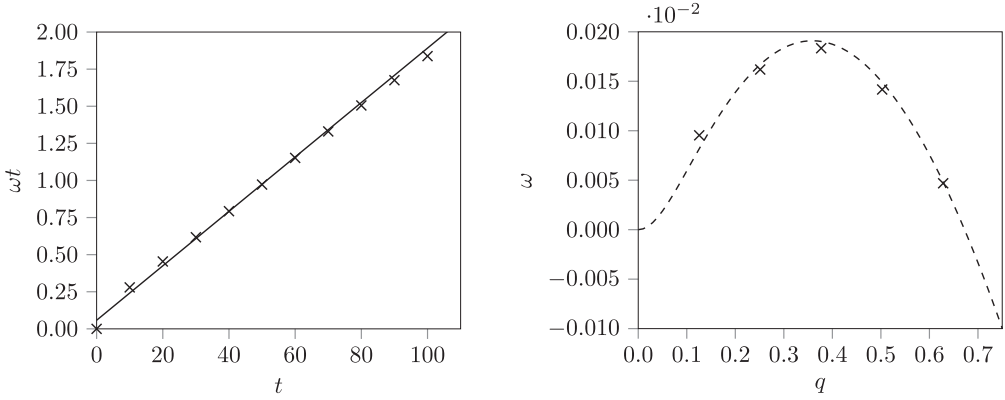
$$n(\xi_r, \theta, 0) = n_0(\xi_r - R_0) + \varepsilon n_1(\xi_r - R_0) f_p(\theta), \quad (5.6b)$$

$$g(\xi_r, \theta, 0) = g_0(\xi_r - R_0) + \varepsilon g_1(\xi_r - R_0) f_p(\theta), \quad (5.6c)$$

where  $\theta \in [0, 2\pi]$ ,  $R_0$  is the initial radius of the unperturbed colony, and correction functions  $n_1$  and  $g_1$  correspond to the theoretically most unstable wave number. The perturbation function takes the form

$$f_p(\theta) = \sum_{\kappa=2}^{12} \alpha_\kappa \cos(\kappa\theta), \quad (5.7)$$

which represents perturbations with  $\kappa$  petals of amplitude  $\alpha_\kappa$  for  $\kappa = 2, \dots, 12$ . We draw each of the coefficients  $\alpha_\kappa$  randomly from the continuous uniform distribution  $U(-1, 1)$ , and then normalise them such that  $f_p(\theta) \in [-1, 1]$ . This ensures that  $\varepsilon$  represents the maximum perturbation amplitude. Based on the experimental length and time scales calculated in Section 3.1, the end of



(a) Linear regression to calculate  $\omega$  from (5.5), for  $q = 0.3770$ . The coefficient of determination is  $r^2 = 0.9958$ .

(b) The dispersion relation for  $D = 0.470$  computed numerically.

**Fig. 5.3.** Calculation of the growth rate and dispersion relation for  $D = 0.470$ , and  $\varepsilon = 0.1$ .

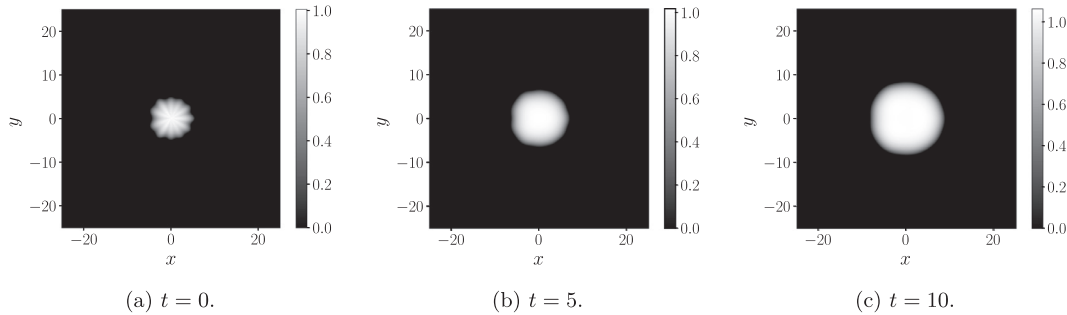


**Fig. 5.4.** Numerical solutions to (5.1) using the initial condition (5.6), for  $D = 0.47$ ,  $\varepsilon = 0.5$ , and  $R_0 = 5$ .

the experiment corresponds to a dimensionless time of  $\hat{t} = 20.1$ , at which time the mean dimensionless mat radius is  $\hat{r} = 7.02$ . To ensure that the numerical solutions are on an appropriate scale, we choose  $R_0 = 5$  and compute solutions for  $t \in [0, 10]$ . We then compare these solutions with experimental results and linear stability analysis predictions.

To determine whether we observe petal formation in the solutions, we compute the spectrum (2.1) of the angular pair-correlation function of images of the numerical solutions. For a given  $\kappa$ , if the amplitude of the power spectrum  $\hat{f}_\kappa^2$  increases over time, we conclude that the wave number corresponding to  $\kappa$  petals is unstable. Alternatively, if the amplitude of  $\hat{f}_\kappa^2$  decreases, we conclude that the relevant mode is stable. To illustrate this process, we plot a numerical solution, binary images, and the corresponding power spectrum for  $D = 0.47$ , and  $t \in \{0, 5, 10\}$  in Figs. 5.4, 5.5 and 5.6, respectively.

As Fig. 5.6 shows, the magnitude of the power spectrum increases for the modes  $\kappa \in \{2, 3, 4\}$ , and decreases for modes  $\kappa \geq 5$ . As we impose random perturbations, we repeat these computations several times for  $D = 0.181$ ,  $D = 0.47$ , and  $D = 1.02$  to ensure that all modes are adequately represented. Analysing repeated solutions, we find that modes for  $\kappa \in \{2, 3, 4, 5, 6\}$  are unstable for  $D = 0.181$ , the modes  $\kappa \in \{2, 3, 4\}$  are unstable for  $D = 0.47$ , and the modes  $\kappa \in \{2, 3\}$  are unstable for  $D = 1.02$ . Qualitatively, this agrees well with the dispersion relations computed in Fig. 5.1, where there is a range of unstable modes for all of  $D = 0.181$ ,  $D = 0.47$ , and  $D = 1.02$ . Furthermore, the widest range of unstable modes occurs for  $D = 0.181$ , and the narrowest for  $D = 1.02$ , which also agrees with the theory. The results for mean data with  $D = 0.47$  also agree well with the experimental power spectra in Fig. A.5, in which the modes  $\kappa \in \{2, 3, 4\}$ , are predominantly re-

sented. This provides evidence that our proposed nutrient-limited growth mechanism is a plausible explanation for the experimentally observed floral pattern formation in circular geometry.

## 6. Discussion

In this work, our objective was to determine the extent to which nutrient-limited growth alone could explain pattern formation in mat biofilms of the yeast *S. cerevisiae*. To test this hypothesis, we used experimental data to parameterise a reaction-diffusion model with non-linear cell diffusion. We showed that the model predicts that the small perturbations inherent to experiments can grow into petal-like structures. This, and supporting numerical solutions, provided evidence that nutrient-limited growth is a plausible mechanism for petal formation in yeast mat biofilms. However, it is important to consider some limitations of our study when interpreting the results.

A common issue with cell growth experiments is that wide biological variation is possible, which can render them difficult to reproduce. Indeed, although all of the quantities measured remain of the same order of magnitude across the thirteen experiments, these variations make determining the experimental parameters difficult. We have therefore adopted several assumptions to obtain estimates. These include assuming that cell density is constant at the end of the experiment, and calculating the proliferation rate by assuming the absence of diffusion. In our numerical solutions, we also only perturb prescribed modes at a single radius, whereas in an experiment the mat is continually subjected to perturbations as it grows. Owing to these difficulties, we can only claim that the model provides mechanistic insight into yeast mat pattern forma-

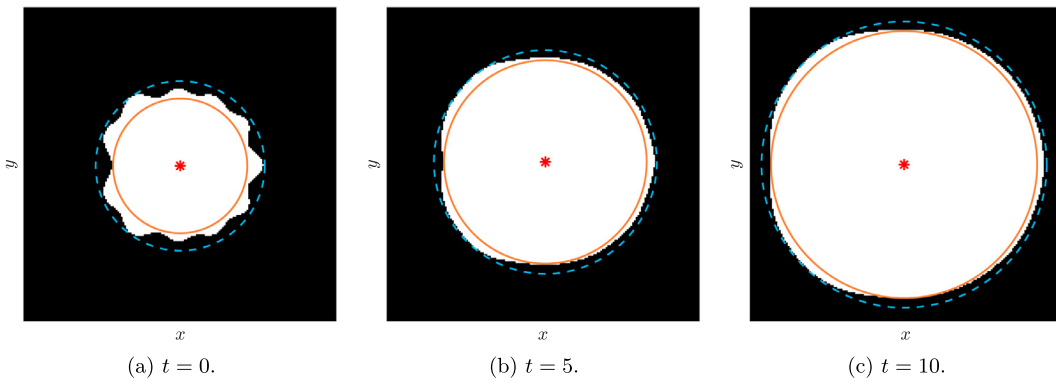


**Fig. 5.5.** Processed binary images of the numerical solutions in Fig. 5.4, indicating the mat centroid (red asterisk), the inner radius (solid orange line), and the outer radius (dashed blue line). (For interpretation of the references to colour in this figure legend, the reader is referred to the web version of this article.)

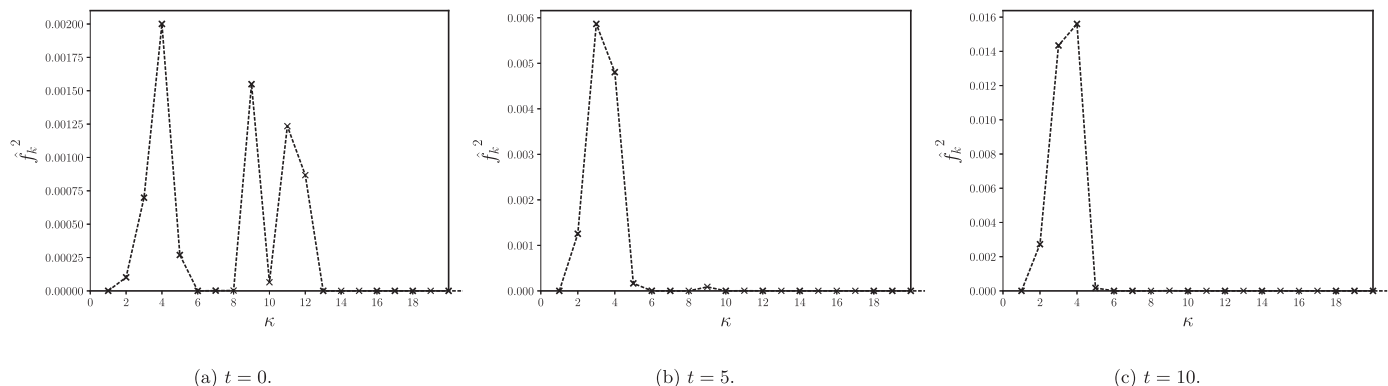


**Fig. 5.6.** Corresponding power spectra of the numerical solutions in Fig. 5.4.

tion, as it cannot recreate the observed patterns with complete fidelity.

Due to the nature of our experiments, we are able to employ a simpler modelling framework than in traditional models of bacterial biofilms, which consider growth on an immersed, non-reactive substratum (Dockery and Klapper, 2001; Eberl et al., 2001; Picioreanu et al., 1998; Rahman et al., 2015; Ward and King, 2012; Ward et al., 2003). For example, as yeast mats receive nutrients readily from the substratum, we do not consider nutrient uptake from a liquid culture medium, which these studies show can affect pattern formation (Dockery and Klapper, 2001; Eberl et al., 2001; Picioreanu et al., 1998). Also, as mats expand due to budding of living cells at their perimeter, we do not consider cell decay, or volume filling effects (Rahman et al., 2015). However, yeast mat biofilms are still highly complex systems, and we cannot hope to have captured all of the mechanisms that contribute to their pattern formation in our minimal model. Although we showed that it is not necessary to invoke other mechanisms to explain the floral pattern, the model considered here provides a framework onto which additional features can be added. In particular, there are mechanical interactions between cells and their environment that are also hypothesised to contribute to the floral patterns. For example, flow of extracellular fluid may provide another means of mat expansion, in addition to the non-linear diffusion and proliferation mechanisms (Lega and Passot, 2003; Ward and King, 2012). Cell adhesion to the agar substrate also causes wrinkling within the agar, which appears to be aligned preferentially with the petals (Chen et al., 2014). We defer investigation of these mechanical effects to future work.

## 7. Conclusion

Yeast biofilms have a myriad of effects on human life. In many applications, it would be advantageous to develop methods to control their growth. For example, yeast biofilms are often found on implanted medical devices, which makes them a leading cause of persistent hospital-acquired infections. There is also strong interest in controlling growth to improve outcomes, for example, in food and drink production and biotechnology, where yeasts are widely used. Furthermore, as a simple eukaryotic organism, yeast is often used as a model for investigating the behaviour of more complex plant and animal cells. It is therefore of interest to develop methods to quantify the growth of yeast biofilms, and to understand the mechanisms that govern their morphology. In this work, we contribute to both of these objectives. Using a radial metric, we show that a mat expands radially at a roughly constant speed, and quantify the transition to floral morphology using an angular pair-correlation function. Using geometric singular perturbation theory and numerics, we demonstrate that a minimal reaction-diffusion model for nutrient-limited yeast growth admits travelling wave solutions, with a minimum speed dependent only on the ratio of diffusion coefficients. Linear stability analysis shows that such travelling wave solutions are unstable to transverse perturbations for experimentally feasible parameters. We find good agreement between this analysis, numerical solutions, and experimental data, allowing us to conclude that nutrient-limited growth is a possible mechanism by which yeast mats attain their floral morphology.

## 8. Acknowledgements

A. T. would like to acknowledge funding support from the A. F. Pillow Applied Mathematics Trust, and from the Australian Government under the Research Training Program. J. E. F. G. acknowledges funding from an ARC Discovery Early Career Researcher Award (DE130100031). S. B. acknowledges funding from an ARC Future Fellowship (FT130100484). B. J. B. would like to acknowledge funding provided by the Australian government under the [Australian Research Council](#) (ARC) Discovery project DP160102644. E. L. T. was supported by an Adelaide Graduate Research Scholarship (University of Adelaide) and funding from [Wine Australia](#) (GWR Ph1305). J. M. G. and J. F. S. were supported by ARC Discovery Project DP130103547 awarded to V. J. This work was supported with supercomputing resources provided by the Phoenix High Performance Computing service at the University of Adelaide. The au-

thors wish to acknowledge several helpful comments from anonymous referees that contributed significant improvements to this research.

## 9. Author contributions

All authors designed the research. A. T. performed the image analysis and mathematical modelling, with assistance from B. J. B., J. E. F. G., and S. B., and wrote the manuscript. E. L. T., J. M. G., and J. F. S. performed the mat formation experiments under supervision of V. J., and collected the data. All authors provided comments and guidance on the manuscript.

## Appendix A. Mat biofilm images

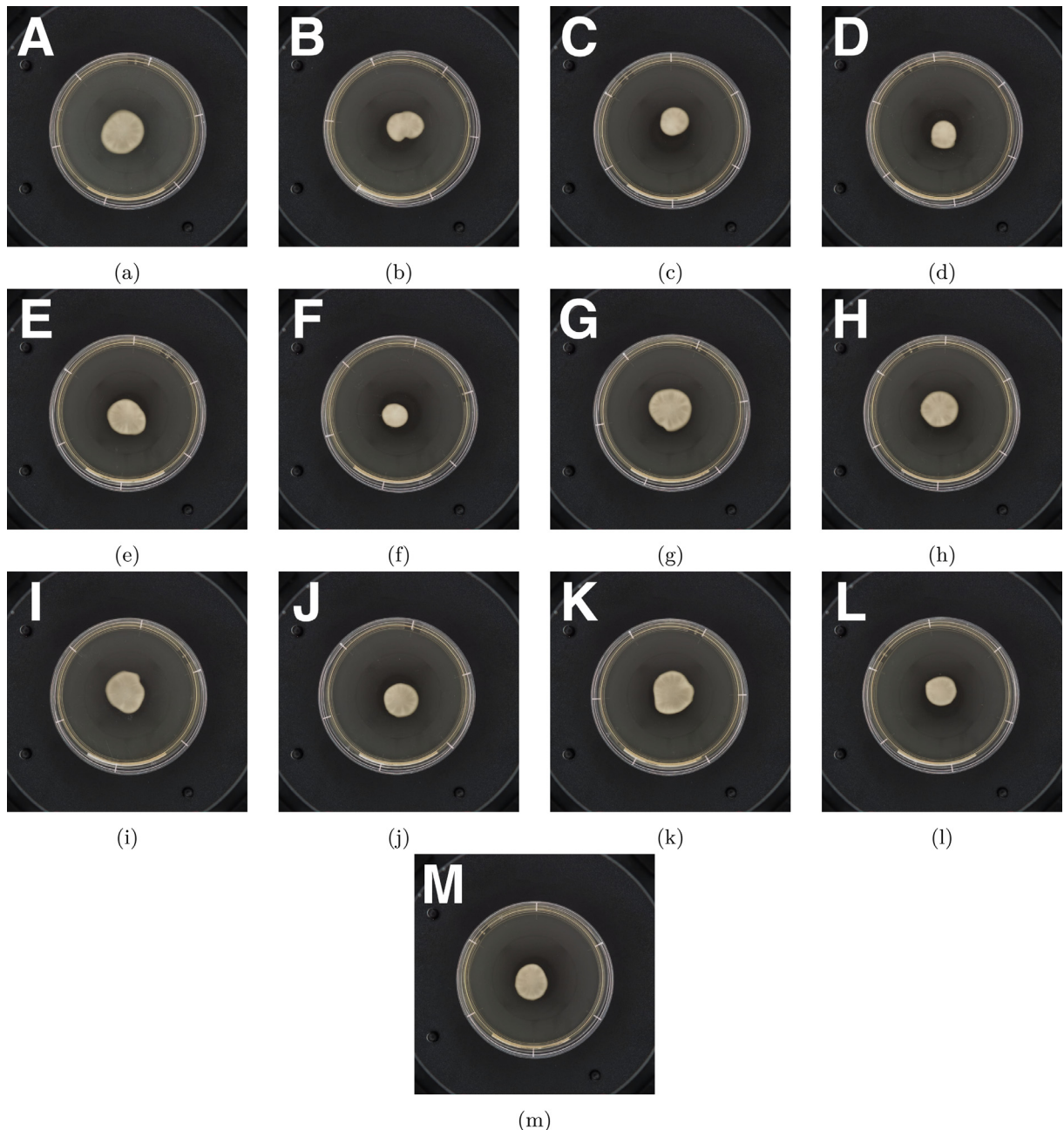


**Fig. A.1.** Photographs of the mat formation experiments, taken  $t = 4099 \text{ min} \approx 68 \text{ h}$  after inoculation.

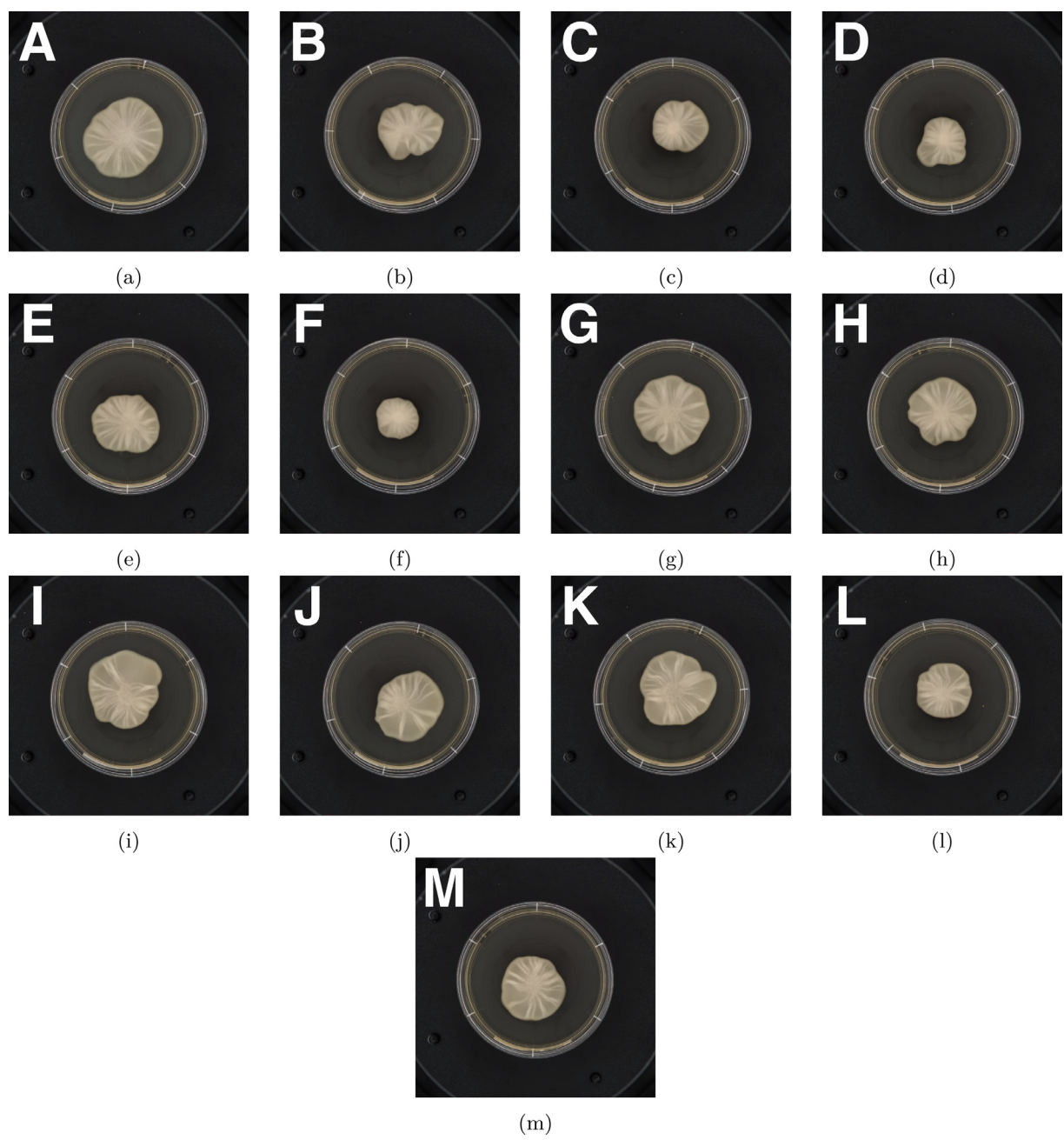


**Fig. A.2.** Photographs of the mat formation experiments, taken  $t = 7013 \text{ min} \approx 117 \text{ h}$  after inoculation.

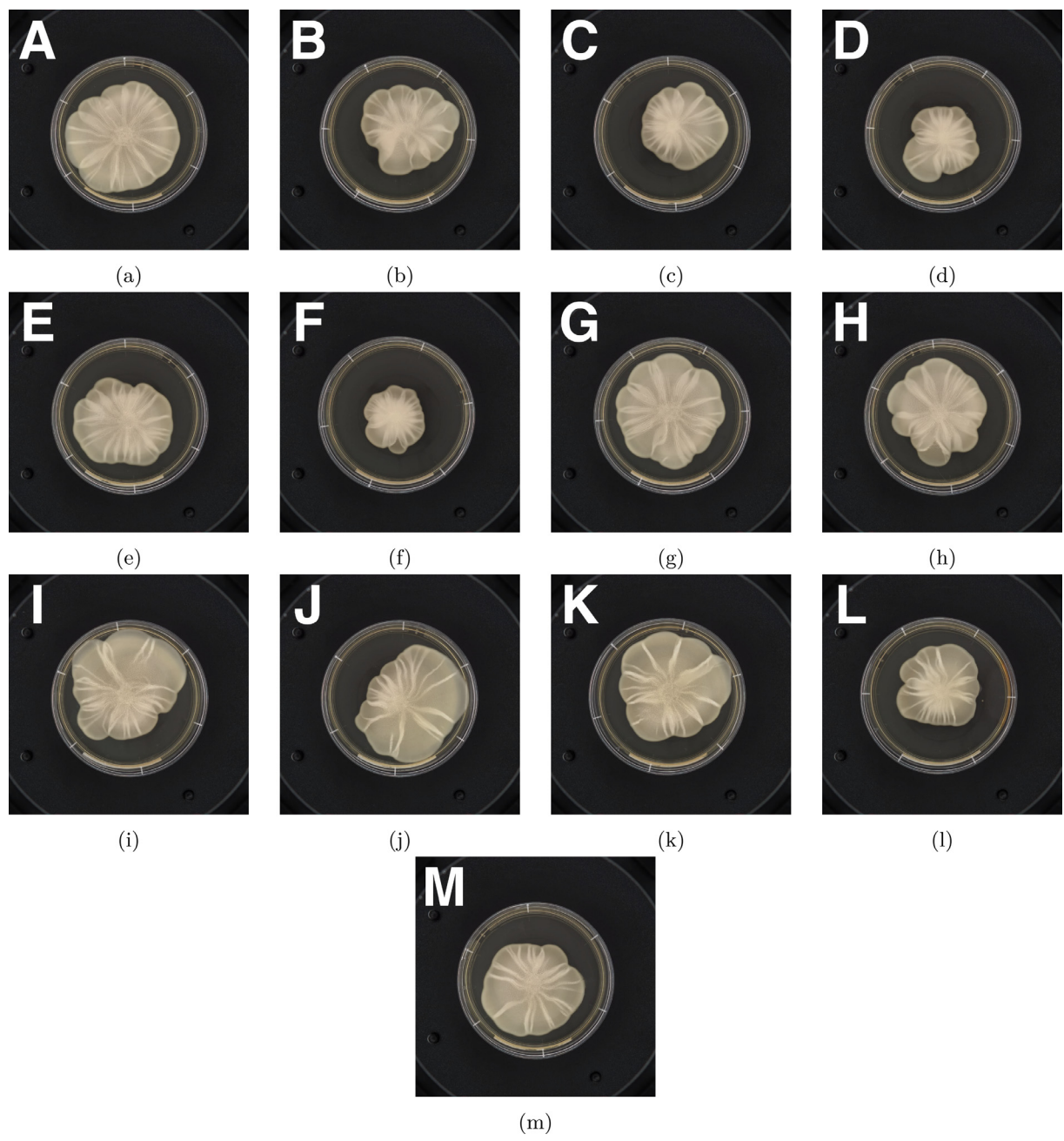


**Fig. A.3.** Photographs of the mat formation experiments, taken  $t = 9866 \text{ min} \approx 164 \text{ h}$  after inoculation.

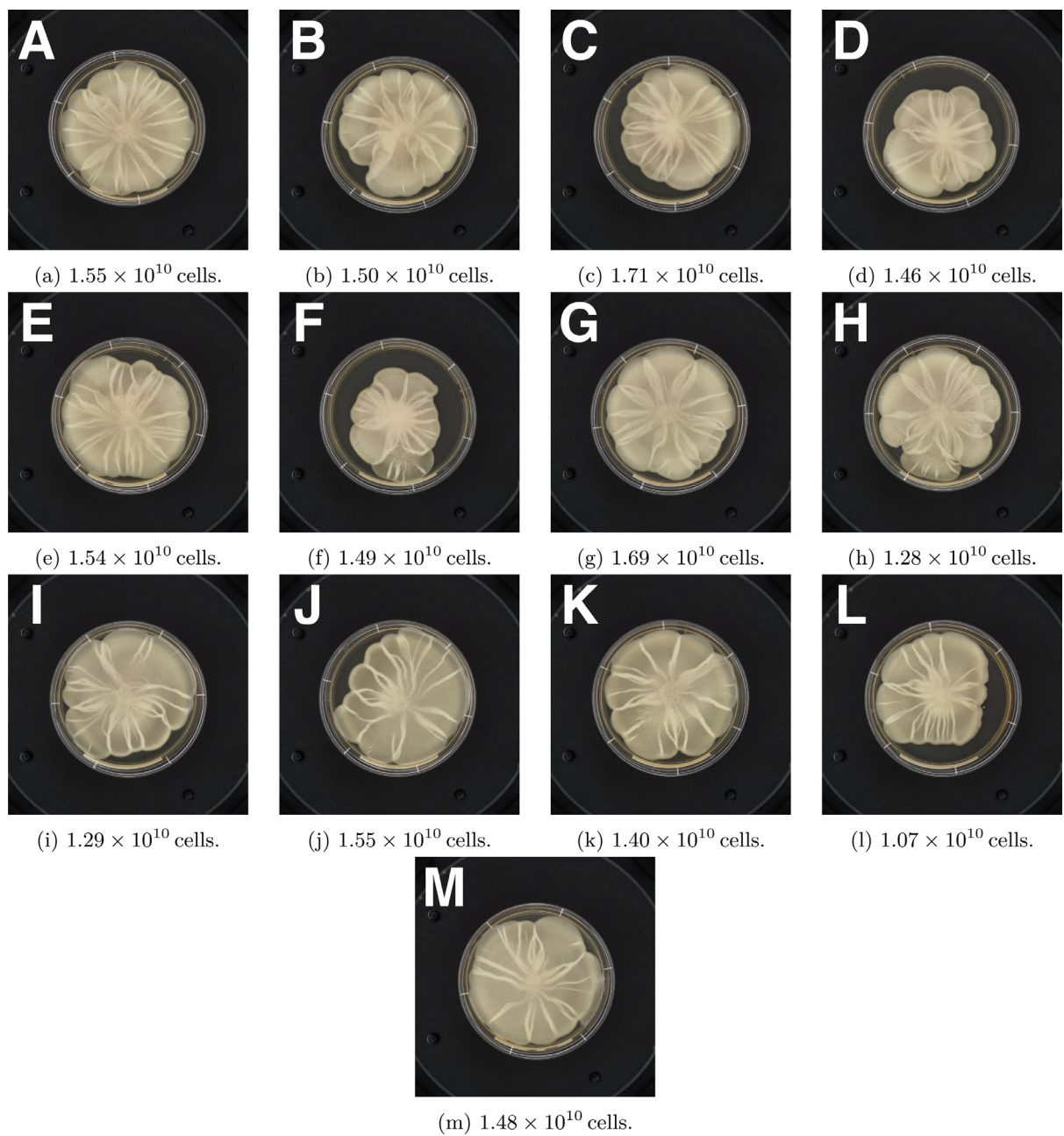


**Fig. A.4.** Photographs of the mat formation experiments, taken at the end of the experiment,  $t = 14208\text{ min} \approx 237\text{ h}$  after inoculation. The approximate cell count for each mat is given in the caption.

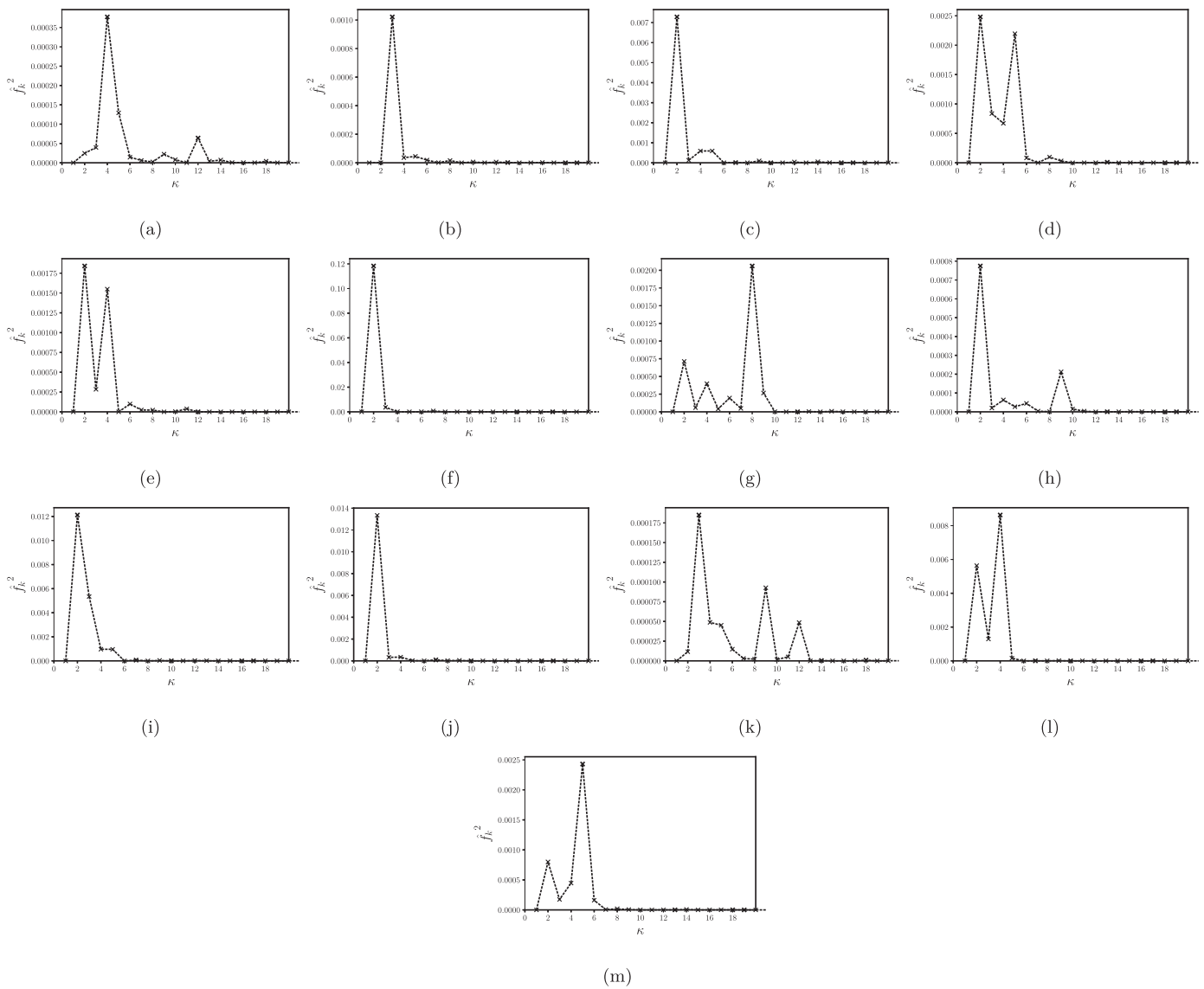


**Fig. A.5.** Power spectra of the angular pair-correlation functions computed from the mat images in Fig. A.4, taken at the end of the mat formation experiment.

## Appendix B. Estimation of dimensional parameters

Here, we describe the methods of estimating  $D_g$ ,  $\mathcal{G}$ ,  $\mathcal{N}$ ,  $c$ , and  $p$ , the relevant dimensional parameters in the model.

### B1. Glucose diffusion coefficient

To estimate the glucose diffusivity in agar, we use the empirical relationship given by (Slade et al., 1966),

$$\frac{D_g}{D_0} = 1 - 0.023w, \quad (\text{B.1})$$

where  $D_0 = 4.04 \times 10^{-2} \text{ mm}^2 \text{ min}^{-1}$  is the diffusivity of glucose in water (Longsworth, 1955), and  $w$  is the weight percentage of the agar. The agar concentration of the medium in which the glucose is placed was 0.3% in each experiment, and therefore the estimate of glucose diffusivity is

$$D_g = 4.01 \times 10^{-2} \text{ mm}^2 \text{ min}^{-1}. \quad (\text{B.2})$$

### B2. Initial glucose concentration

In our scaling, we use the initial concentration of glucose as the reference glucose concentration,  $\mathcal{G}$ . The initial mass of glucose added to each plate was 0.5 g, and the agar medium occupies a circular area with diameter of approximately 83 mm. From this, we determine that the initial concentration of glucose in each experiment was

$$\mathcal{G} = 9.24 \times 10^{-5} \text{ g mm}^{-2}. \quad (\text{B.3})$$

### B3. Final cell density

In each experiment, we could only measure the cell density at the end of the experiment, as doing so destroyed the biofilm. Therefore, we use the mean cell density at the end of the experiment as the reference cell density,  $\mathcal{N}$ . At the conclusion of each experiment, we estimated the total number of cells by washing the mat from the medium, and counting the number of cells in a small sample of the washed material. From this, we obtained a mean of  $1.46 \times 10^{10}$  cells per mat. By analysing processed images in Matlab, we found that the mats have a mean area of  $4.46 \times 10^3 \text{ mm}^2$  at

the conclusion of the experiment. The mean reference cell density from the experiments was therefore

$$\mathcal{N} = 3.34 \times 10^6 \text{ cells mm}^{-2}. \quad (\text{B.4})$$

#### B4. Quantity of glucose consumed per new cell

To estimate  $c$ , we assume that all of the consumed glucose is used for the creation of new cells, giving the dimensionless parameter  $\Upsilon = 1$ . In addition, we assume that all of the glucose is consumed by the end of the experiment. An estimate of the quantity of glucose consumed per new cell is therefore

$$c = \frac{\mathcal{G}}{\mathcal{N}} = 2.77 \times 10^{-11} \text{ g} \cdot \text{cell}^{-1}. \quad (\text{B.5})$$

#### B5. Cell proliferation rate

The cell proliferation rate,  $p$ , is not directly measurable, and is therefore the most difficult parameter to estimate from the experiments. To obtain an order of magnitude estimate, we isolate  $p$  by considering the dimensional model equations (3.2) in the absence of diffusion,

$$\frac{\partial n}{\partial t} = p n g, \quad (\text{B.6a})$$

$$\frac{\partial g}{\partial t} = -c p n g. \quad (\text{B.6b})$$

If we add multiply equation (B.6a) by the constant  $c$ , add the result to (B.6b), and integrate once with respect to  $t$ , we obtain the conserved quantity  $cn + g = c\mathcal{N}_0 + \mathcal{G}$ , where  $\mathcal{N}_0 = n(0)$  is the initial cell density. Hence, we can rewrite the equation for the number of cells as

$$\frac{\partial n}{\partial t} = pn(c\mathcal{N}_0 + \mathcal{G} - cn). \quad (\text{B.7})$$

Eq. (B.7) is a first-order, non-linear, Bernoulli ordinary differential equation, which has the solution

$$n(t) = \frac{\mathcal{N}_0(c\mathcal{N}_0 + \mathcal{G})e^{pt(c\mathcal{N}_0 + \mathcal{G})}}{c\mathcal{N}_0e^{pt(c\mathcal{N}_0 + \mathcal{G})} + \mathcal{G}}. \quad (\text{B.8})$$

In each experiment, 5000 cells were initially placed in the Petri dish, concentrated in circular regions with a mean diameter of 5.75 mm. We therefore estimate the initial cell density as  $\mathcal{N}_0 = 144.5 \text{ cells mm}^{-2}$ . The final cell density,  $n(t)$ , is the mean cell density at the end of the experiment,  $\mathcal{N}$ . We can then obtain an estimate for the cell proliferation rate by rearranging (B.8) to give

$$p = \frac{\mathcal{N}}{14208\mathcal{G}(\mathcal{N}_0 + \mathcal{N})} \log\left(\frac{\mathcal{N}^2}{\mathcal{N}_0^2}\right). \quad (\text{B.9})$$

Using the experimental parameters already determined, our cell proliferation rate estimate is

$$p = 15.28 \text{ mm}^2 \text{ g}^{-1} \text{ min}^{-1}. \quad (\text{B.10})$$

We note that as this model neglects diffusion, this value is likely to over-estimate the true proliferation rate, and should therefore be considered to be an upper bound for  $p$ .

#### Appendix C. Numerical method

Here, we describe the numerical method we use to solve the model equations (5.1) in two-dimensional Cartesian co-ordinates. We compute solutions on an equispaced discrete domain, where  $\Delta x$  and  $\Delta y$  are the constant  $x$  and  $y$  grid spacing, respectively, and  $\Delta t$  is the constant time step size. We denote the cell density  $n_{i,j}^k = n(x_i, y_j, t_k)$  and nutrient concentration  $g_{i,j}^k = g(x_i, y_j, t_k)$ ,

where  $i = 1, \dots, N_x$ ,  $j = 1, \dots, N_y$ , and  $k = 1, \dots, N_t$  are indices of grid points  $x_i$  and  $y_j$ , and time steps  $t_k$ , respectively. To discretise the equations, we employ a second-order accurate central finite difference scheme in space, and a Crank–Nicolson scheme for time stepping. We linearise the equations by approximating the non-linear terms using known data from the previous time step. Under this scheme, discretising the model equations (5.1) yields

$$\begin{aligned} \frac{n_{i,j}^{k+1} - n_{i,j}^k}{\Delta t} &= \frac{D}{2} \left[ \frac{n_{i,j}^k + n_{i+1,j}^k}{2\Delta x^2} n_{i+1,j}^{k+1} - \frac{n_{i+1,j}^k + 2n_{i,j}^k + n_{i-1,j}^k}{2\Delta x^2} n_{i,j}^{k+1} \right. \\ &\quad + \frac{n_{i,j}^k + n_{i-1,j}^k}{2\Delta x^2} n_{i-1,j}^{k+1} + \frac{n_{i,j}^k + n_{i+1,j}^k}{2\Delta x^2} n_{i+1,j}^k \\ &\quad \left. - \frac{n_{i+1,j}^k + 2n_{i,j}^k + n_{i-1,j}^k}{2\Delta x^2} n_{i,j}^k + \frac{n_{i,j}^k + n_{i-1,j}^k}{2\Delta x^2} n_{i-1,j}^k \right] \\ &\quad + \frac{D}{2} \left[ \frac{n_{i,j}^k + n_{i,j+1}^k}{2\Delta y^2} n_{i,j+1}^{k+1} - \frac{n_{i,j+1}^k + 2n_{i,j}^k + n_{i,j-1}^k}{2\Delta y^2} n_{i,j}^{k+1} \right. \\ &\quad + \frac{n_{i,j}^k + n_{i,j-1}^k}{2\Delta y^2} n_{i,j-1}^{k+1} + \frac{n_{i,j}^k + n_{i,j+1}^k}{2\Delta y^2} n_{i,j+1}^k \\ &\quad \left. - \frac{n_{i,j+1}^k + 2n_{i,j}^k + n_{i,j-1}^k}{2\Delta y^2} n_{i,j}^k + \frac{n_{i,j}^k + n_{i,j-1}^k}{2\Delta y^2} n_{i,j-1}^k \right] \\ &\quad + \frac{1}{2} [n_{i,j}^{k+1} g_{i,j}^k + n_{i,j}^k g_{i,j}^k], \end{aligned} \quad (\text{C.1a})$$

$$\begin{aligned} \frac{g_{i,j}^{k+1} - g_{i,j}^k}{\Delta t} &= \frac{1}{2} \left[ \frac{g_{i+1,j}^{k+1} - 2g_{i,j}^{k+1} + g_{i-1,j}^{k+1}}{\Delta x^2} + \frac{g_{i+1,j}^k - 2g_{i,j}^k + g_{i-1,j}^k}{\Delta x^2} \right] \\ &\quad + \frac{1}{2} \left[ \frac{g_{i,j+1}^{k+1} - 2g_{i,j}^{k+1} + g_{i,j-1}^{k+1}}{\Delta y^2} + \frac{g_{i,j+1}^k - 2g_{i,j}^k + g_{i,j-1}^k}{\Delta y^2} \right] \\ &\quad - \frac{1}{2} [n_{i,j}^k g_{i,j}^{k+1} + n_{i,j}^k g_{i,j}^k]. \end{aligned} \quad (\text{C.1b})$$

We enforce periodic conditions on all spatial boundaries by defining ghost points such that  $n_{0,j}^k = n_{N_x,j}^k$ ,  $n_{N_x+1,j}^k = n_{1,j}^k$ , and so on, applying these in (C.1) at the relevant boundary points.

The discretised equations (C.1) define a problem that we can solve implicitly for the  $2N_x N_y$  unknowns  $n_{i,j}^{k+1}$  and  $g_{i,j}^{k+1}$ , given knowledge of the solution at the previous time step,  $n_{i,j}^k$  and  $g_{i,j}^k$ . We use the generalised minimal residual (GMRES) method to solve this system of equations at each time step. GMRES is an iterative method for solving linear systems  $A\vec{x} = \vec{b}$ , whereby the exact solution is approximated by the vector in the  $n^{\text{th}}$  Krylov subspace,

$$\vec{x}_n \in K_n = \text{span}\{\vec{b}, A\vec{b}, A^2\vec{b}, \dots, A^{n-1}\vec{b}\}, \quad (\text{C.2})$$

that minimises the Euclidean norm of the residual  $\vec{r}_n = A\vec{x}_n - \vec{b}$  (Saad and Schultz, 1986). An advantage of the method is that there is no need to define the matrix  $A$  explicitly, and we instead proceed by defining the matrix–vector product  $A\vec{x}$ , and the known vector  $\vec{b}$  at each time step. At each time step, we accept the solution if the residual  $\|\vec{r}_n\| < 1 \times 10^{-6}$ .

To determine an appropriate grid spacing and time step size, we perform a grid convergence study using the test value of  $D = 0.47$ , which has a theoretical wave speed of  $v = 0.34794$ . In our tests, we solve (5.1) for  $t \in [0, 100]$  using the theoretical travelling wave profiles as initial conditions, and compute the mean speed at which the front advances in the numerical solution. In these tests, the numerical method produces a solution with the theoretical wave speed when  $\Delta x = \Delta y = 0.1$ , and  $\Delta t = 0.001$ . Convergence results using these values are shown in Fig. C.1. The numerical scheme exhibits approximately quadratic convergence with grid spacing

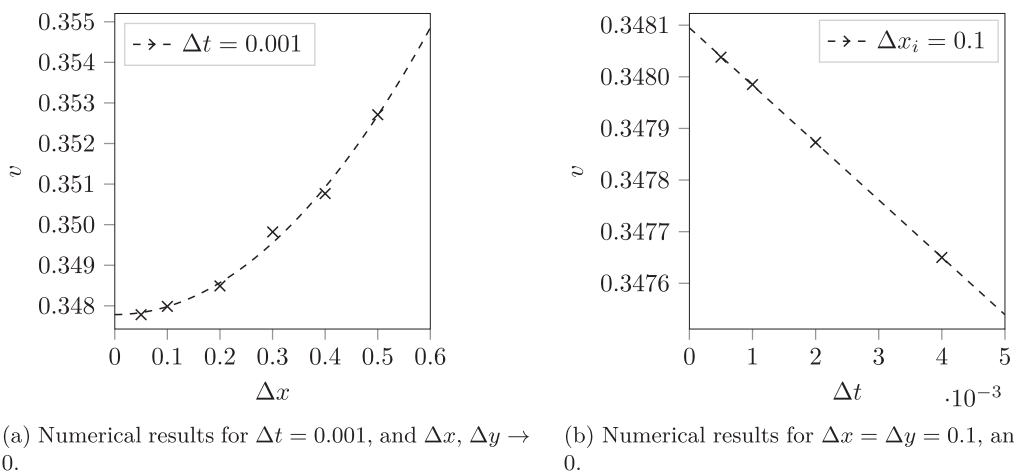


**Fig. C.1.** Numerical convergence results for the scheme (C.1), solved with the GMRES iterative method. For each data point, we plot the mean wave speed computed at  $t = 100$ .

and linear convergence with time step size. By fitting an appropriate polynomial to the data in Fig. C.1(a) and (b) and extrapolating, we can estimate the numerical wave speed in the zero grid spacing and time step limit respectively. Doing so, we find that when  $\Delta t = 0.001$ , the estimated wave speed as  $\Delta x_i \rightarrow 0$  is  $v = 0.34778$ . When  $\Delta x_i = 0.1$ , the estimated wave speed as  $\Delta t \rightarrow 0$  is  $v = 0.34809$ . As these are both accurate to within 0.05% of the theoretical value, we adopt  $\Delta x = \Delta y = 0.1$  and  $\Delta t = 0.001$  in all numerical solutions.

## References

- Alligood, K.T., Sauer, T.D., Yorke, J.A., 1996. Chaos: An Introduction to Dynamical Systems. Springer, New York doi:[10.1007/b97589](https://doi.org/10.1007/b97589).
- Aronson, D.G., 1980. Density-dependent interaction-diffusion systems. In: Stewart, W.E., Ray, W.H., Conley, C.C. (Eds.), Dynamics and Modelling of Reactive Systems, 44. Academic Press, New York-London, pp. 161–176. doi:[10.1016/B978-0-12-669550-2.50010-5](https://doi.org/10.1016/B978-0-12-669550-2.50010-5).
- Asally, M., Kittisopikul, M., Rué, P., Du, Y., Hu, Z., Çağatay, T., Robinson, A.B., Lu, H., Garcia-Ojalvo, J., Süel, G.M., 2012. Localized cell death focuses mechanical forces during 3D patterning in a biofilm. Proc. Natl. Acad. Sci. U.S.A. 109 (46), 18891–18896. doi:[10.1073/pnas.1212429109](https://doi.org/10.1073/pnas.1212429109).
- Balasuriya, S., Gottwald, G., Hornibrook, J., Lafortune, S., 2007. High Lewis number combustion wavefront: a perturbative Melnikov analysis. SIAM J. Appl. Math. 67 (2), 464–486. doi:[10.1137/050640849](https://doi.org/10.1137/050640849).
- Beauvais, A., Loussert, C., Prevost, M.C., Verstrepen, K., Latgé, J.P., 2009. Characterization of a biofilm-like extracellular matrix in FLO1-expressing *Saccharomyces cerevisiae* cells. FEMS Yeast Res. 9 (3), 411–419. doi:[10.1111/j.1567-1364.2009.00482.x](https://doi.org/10.1111/j.1567-1364.2009.00482.x).
- Ben-Jacob, E., Cohen, I., Levine, H., 2000. Co-operative self organisation in micro-organisms. Adv. Phys. 49 (4), 395–554. doi:[10.1080/000187300405228](https://doi.org/10.1080/000187300405228).
- Billingham, J., Needham, D.J., 1991. The development of travelling waves in quadratic and cubic autocatalysis with unequal diffusion rates. I. Permanent form traveling waves. Philos. Trans. R. Soc. Lond. 334 (1633), 1–24. doi:[10.1088/rsta.1991.0001](https://doi.org/10.1088/rsta.1991.0001).
- Binder, B.J., Sundstrom, J.F., Gardner, J.M., Jiranek, V., Oliver, S.G., 2015. Quantifying two-dimensional filamentous and invasive growth spatial patterns in yeast colonies. PLoS Comput. Biol. 11 (2), e1004070. doi:[10.1371/journal.pcbi.1004070](https://doi.org/10.1371/journal.pcbi.1004070).
- Chen, L., Noorbakhsh, J., Adams, R.M., Samaniego-Evans, J., Agollah, G., Nevozhay, D., Kuzdzal-Fick, J., Mehta, P., Balázs, G., 2014. Two-dimensionality of yeast colony expansion accompanied by pattern formation. PLoS Comput. Biol. 10 (12), e1003979. doi:[10.1371/journal.pcbi.1003979](https://doi.org/10.1371/journal.pcbi.1003979).
- Dockery, J., Klapper, I., 2001. Finger formation in biofilm layers. SIAM J. Appl. Math. 62 (3), 853–869. doi:[10.1137/s0036139900371709](https://doi.org/10.1137/s0036139900371709).
- Eberl, H.J., Parker, D.F., van Loosdrecht, M.C.M., 2001. A new deterministic spatio-temporal continuum model for biofilm development. J. Theor. Med. 3 (3), 161–175. doi:[10.1080/10273660108833072](https://doi.org/10.1080/10273660108833072).
- Edelstein-Keshet, L., 1988. Mathematical Models in Biology. Society for Industrial and Applied Mathematics doi:[10.1137/1.9780898719147](https://doi.org/10.1137/1.9780898719147).
- Fenichel, N., 1979. Geometric singular perturbation theory for ordinary differential equations. J. Differ. Equ. 31 (1), 53–98. doi:[10.1016/0022-0396\(79\)90152-9](https://doi.org/10.1016/0022-0396(79)90152-9).
- Francisco Leyva, J., Málaga, C., Plaza, R.G., 2013. The effects of nutrient chemotaxis on bacterial aggregation patterns with non-linear degenerate cross diffusion. Phys. A Stat. Mech. Appl. 392 (22), 5644–5662. doi:[10.1016/j.physa.2013.07.022](https://doi.org/10.1016/j.physa.2013.07.022).
- Gallegos, A., Mazzag, B., Mogilner, A., 2006. Two continuum models for the spreading of myxobacteria swarms. Bull. Math. Biol. 68 (4), 837–861. doi:[10.1007/s11538-005-9031-2](https://doi.org/10.1007/s11538-005-9031-2).
- Giverso, C., Verani, M., Ciarletta, P., 2015. Branching instability in expanding bacterial colonies. J. R. Soc. Interface 12 (104), 20141290. doi:[10.1098/rsif.2014.1290](https://doi.org/10.1098/rsif.2014.1290).
- Goffeau, A., Barrell, B.G., Bussey, H., Davis, R.W., Dujon, B., Feldmann, H., Galibert, F., Hoheisel, J.D., Jacq, C., Johnston, M., Louis, E.J., Mewes, H.W., Murakami, Y., Philippsen, P., Tettelin, H., Oliver, S.G., 1996. Life with 6000 genes. Science 274 (5287), 546–567. doi:[10.1126/science.274.5287.546](https://doi.org/10.1126/science.274.5287.546).
- Gray, B.F., Kirwan, N.A., 1974. Growth rates of yeast colonies on solid media. Biophys. Chem. 1 (3), 204–213. doi:[10.1016/0301-4622\(74\)80006-2](https://doi.org/10.1016/0301-4622(74)80006-2).
- Grindrod, P., 1991. Patterns and Waves: The Theory and Applications of Reaction-Diffusion Equations. Oxford University Press.
- Harley, K., van Heijster, P., Marangell, R., Pettet, G.J., Wechselberger, M., 2014. Existence of travelling wave solutions for a model of tumor invasion. SIAM J. Appl. Dyn. Syst. 13 (1), 366–396. doi:[10.1137/130923129](https://doi.org/10.1137/130923129).
- Hilhorst, D., Kersner, R., Logak, E., Mimura, M., 2008. Interface dynamics of the Fisher equation with degenerate diffusion. J. Differ. Equ. 244 (11), 2870–2889. doi:[10.1016/j.jde.2008.02.018](https://doi.org/10.1016/j.jde.2008.02.018).
- Horváth, D., Petrov, V., Scott, S.K., Showalter, K., 1993. Instabilities in propagating reaction-diffusion fronts. J. Chem. Phys. 98 (8), 6332–6343. doi:[10.1063/1.465062](https://doi.org/10.1063/1.465062).
- Johnston, S.T., Simpson, M.J., McElwain, D.L.S., 2014. How much information can be obtained from tracking the position of the leading edge in a scratch assay? J. R. Soc. Interface 11 (97), 20140325. doi:[10.1098/rsif.2014.0325](https://doi.org/10.1098/rsif.2014.0325).
- Jones, C.K.R.T., 1995. Dynamical Systems, 1609. Springer, Berlin, pp. 44–118. doi:[10.1007/bf0095237](https://doi.org/10.1007/bf0095237).
- Kapitula, T., Promislow, K., 2013. Spectral and Dynamical Stability of Nonlinear Waves. Applied Mathematical Sciences, 185. Springer, New York doi:[10.1007/978-1-4614-6995-7](https://doi.org/10.1007/978-1-4614-6995-7).
- Kawasaki, K., Mochizuki, A., Matsushita, M., Umeda, T., Shigesada, N., 1997. Modeling spatio-temporal patterns generated by *Bacillus subtilis*. J. Theor. Biol. 188 (2), 177–185. doi:[10.1006/jtbi.1997.0462](https://doi.org/10.1006/jtbi.1997.0462).
- Kitsunazeaki, S., 1997. Interface dynamics for bacterial colony formation. J. Phys. Soc. Jpn. 66 (5), 1544–1550. doi:[10.1143/jpsj.66.1544](https://doi.org/10.1143/jpsj.66.1544).
- Klapper, I., Dockery, J., 2010. Mathematical description of microbial biofilms. SIAM Rev. 52 (2), 221–265. doi:[10.1137/080739720](https://doi.org/10.1137/080739720).
- Lega, J., Passot, T., 2003. Hydrodynamics of bacterial colonies: a model. Phys. Rev. E 67 (3), 031906. doi:[10.1103/physreve.67.031906](https://doi.org/10.1103/physreve.67.031906).
- Longsworth, L.G., 1955. Electrochemistry in Biology and Medicine. John Wiley & Sons, Inc., New York, N.Y., pp. 225–247. doi:[10.1016/0002-8703\(55\)90290-8](https://doi.org/10.1016/0002-8703(55)90290-8).
- Maini, P.K., McElwain, D.L.S., Leavesley, D.I., 2004. Travelling wave model to interpret a wound-healing cell migration assay for human peritoneal mesothelial cells. Tissue Eng. 10 (3–4), 475–482. doi:[10.1089/107632704323061834](https://doi.org/10.1089/107632704323061834).
- Marchant, B.P., Norbury, J., Sherratt, J.A., 2001. Travelling wave solutions to a haptoxin-dominated model of malignant invasion. Nonlinearity 14 (6), 1653–1671. doi:[10.1088/0951-7715/14/6/313](https://doi.org/10.1088/0951-7715/14/6/313).
- Martinez, L.M., Fries, B.C., 2010. Fungal biofilms: relevance in the setting of human disease. Curr. Fungal Infect. Rep. 4 (4), 266–275. doi:[10.1007/s12281-010-0035-5](https://doi.org/10.1007/s12281-010-0035-5).
- Minois, N., Frajnt, M., Wilson, C., Vaupel, J.W., 2005. Advances in measuring lifespan in the yeast *Saccharomyces cerevisiae*. Proc. Natl. Acad. Sci. U.S.A. 102 (2), 402–406. doi:[10.1073/pnas.0408332102](https://doi.org/10.1073/pnas.0408332102).
- Müller, J., van Saarloos, W., 2002. Morphological instability and dynamics of fronts in bacterial growth models with nonlinear diffusion. Phys. Rev. E 65 (6), 061111. doi:[10.1103/physreve.65.061111](https://doi.org/10.1103/physreve.65.061111).
- Murray, J.D., 2002. Mathematical Biology I: An Introduction, third Springer doi:[10.1007/b98868](https://doi.org/10.1007/b98868).

- Murray, J.D., 2003. Mathematical Biology II: Spatial Models and Biomedical Applications, third Springer doi:[10.1007/b98869](https://doi.org/10.1007/b98869).
- Picioreanu, C., van Loosdrecht, M.C.M., Heijnen, J.J., 1998. Mathematical modeling of biofilm structure with a hybrid differential-discrete cellular automaton approach. *Biotechnol. Bioeng.* 58 (1), 101–116. doi:[10.1002/\(SICI\)1097-0290\(19980405\)58:1<101::AID-BIT11>3.0.CO;2-M](https://doi.org/10.1002/(SICI)1097-0290(19980405)58:1<101::AID-BIT11>3.0.CO;2-M).
- Rahman, K.A., Sudarsan, R., Eberl, H.J., 2015. A mixed-culture biofilm model with cross-diffusion. *Bull. Math. Biol.* 77 (11), 2086–2124. doi:[10.1007/s11538-015-0117-1](https://doi.org/10.1007/s11538-015-0117-1).
- Ramage, G., Mowat, E., Williams, C., Lopez Ribot, J.L., 2010. The Yeast Handbook. Springer-Verlag, Berlin, Heidelberg, pp. 121–144. doi:[10.1007/978-3-642-03150-2\\_6](https://doi.org/10.1007/978-3-642-03150-2_6).
- Reynolds, T.B., Fink, G.R., 2001. Bakers' yeast, a model for fungal biofilm formation. *Science* 291 (5505), 878–881. doi:[10.1126/science.291.5505.878](https://doi.org/10.1126/science.291.5505.878).
- Reynolds, T.B., Jansen, A., Peng, X., Fink, G.R., 2008. Mat formation in *Saccharomyces cerevisiae* requires nutrient and pH gradients. *Eukaryot. Cell* 7 (1), 122–130. doi:[10.1128/ec.00310-06](https://doi.org/10.1128/ec.00310-06).
- Saad, Y., Schultz, M.H., 1986. GMRES: a generalized minimal residual algorithm for solving nonsymmetric linear systems. *SIAM J. Sci. Stat. Comput.* 7 (3), 856–869. doi:[10.1137/0907058](https://doi.org/10.1137/0907058).
- Sivashinsky, G.I., 1977. Diffusion-thermal theory of cellular flames. *Combust. Sci. Technol.* 15 (3–4), 137–146. doi:[10.1080/00102207708946779](https://doi.org/10.1080/00102207708946779).
- Slade, A.L., Cremer, A.E., Thomas, H.C., 1966. The obstruction effect in the self-diffusion coefficients of sodium and cesium in agar gels. *J. Phys. Chem.* 70 (9), 2840–2844. doi:[10.1021/j100881a020](https://doi.org/10.1021/j100881a020).
- Smith, W.P.J., Davit, Y., Osborne, J.M., Kim, W., Foster, K.R., Pitt-Francis, J.M., 2016. Cell morphology drives spatial patterning in microbial communities. *Proc. Natl. Acad. Sci. U.S.A.* 114 (3), E280–E286. doi:[10.1073/pnas.1613007114](https://doi.org/10.1073/pnas.1613007114).
- Tronnolone, H., Gardner, J.M., Sundstrom, J.F., Jiranek, V., Oliver, S.G., Binder, B.J., 2017. Quantifying the dominant growth mechanisms of dimorphic yeast using a lattice-based model. *J. R. Soc. Interface* 14, 20170314. doi:[10.1098/rsif.2017.0314](https://doi.org/10.1098/rsif.2017.0314).
- Tronnolone, H., Tam, A., Szenczi, Z., Green, J.E.F., Balasuriya, S., Tek, E.L., Gardner, J.M., Sundstrom, J.F., Jiranek, V., Oliver, S.G., Binder, B.J., 2018. Diffusion-limited growth of microbial colonies. *Sci. Rep. Accepted*.
- Turing, A.M., 1952. The chemical basis of morphogenesis. *Philos. Trans. R. Soc. Lond. B* 237 (641), 37–72. doi:[10.1098/rstb.1952.0012](https://doi.org/10.1098/rstb.1952.0012).
- Váčová, L., Štovíček, V., Hlaváček, O., Chernyavskiy, O., Štěpánek, L., Kubínová, L., Palková, Z., 2011. Flo11p, drug efflux pumps, and the extracellular matrix cooperate to form biofilm yeast colonies. *J. Cell Biol.* 194 (5), 679–687. doi:[10.1083/jcb.201103129](https://doi.org/10.1083/jcb.201103129).
- Ward, J.P., King, J.R., 2012. Thin-film modelling of biofilm growth and quorum sensing. *J. Eng. Math.* 73 (1), 71–92. doi:[10.1007/s10665-011-9490-4](https://doi.org/10.1007/s10665-011-9490-4).
- Ward, J.P., King, J.R., Koerber, A.J., Croft, J.M., Sockett, R.E., Williams, P., 2003. Early development and quorum sensing in bacterial biofilms. *J. Math. Biol.* 47 (1), 23–55. doi:[10.1007/s00285-002-0190-6](https://doi.org/10.1007/s00285-002-0190-6).
- Xue, C., Budrene, E.O., Othmer, H.G., 2011. Radial and spiral stream formation in *Proteus mirabilis* colonies. *PLoS Comput. Biol.* 7 (12), e1002332. doi:[10.1371/journal.pcbi.1002332](https://doi.org/10.1371/journal.pcbi.1002332).